# Hadron Single- and Multiparticle Measurements to Search for Critical Phenomena in Ultrarelativistic Pb+Pb Collisions

A Dissertation Presented

by

Mikhail Leonidovich KOPYTINE

to

The Graduate School

in Partial Fulfillment of the Requirements

for the Degree of

Doctor of Philosophy

in

Physics

State University of New York
at
Stony Brook

month 200?

State University of New York
at Stony Brook

The Graduate School

Mikhail Leonidovich KOPYTINE

We, the dissertation committee for the above candidate for the Doctor of Philosophy degree, hereby recommend acceptance of the dissertation.

Barbara Jacak (Advisor)
Professor of Physics

Paul Grannis (Chair)
Professor of Physics

Heinz Sorge
Professor of Physics

somebody from somewhere else

This dissertation is accepted by the Graduate School.

Graduate School

# Abstract of the Dissertation

# Hadron Single- and Multiparticle Measurements to Search for Critical Phenomena in Ultrarelativistic Pb+Pb Collisions

by

Mikhail Leonidovich KOPYTINE

Doctor of Philosophy

in

Physics

State University of New York at Stony Brook

200?

In the NA44 Experiment, measured are yields and differential distributions of $K^+$, $K^-$, $\pi^+$, $\pi^-$ in transverse kinetic energy and rapidity, around the center-of-mass rapidity in 158 A GeV/c Pb+Pb collisions at the CERN SPS. A considerable enhancement of $K^+$ production per $\pi$ is observed, as compared to $p+p$ collisions at this energy. To illustrate the importance of secondary hadron rescattering as an enhancement mechanism, we compare strangeness production at the SPS and AGS with predictions of the transport model RQMD.

No spiritual bonds can be imposed externally on those beings who neither fear nor hope, but rather act.

*Baron J. Evola*

# Contents

# List of Figures

# List of Tables

## Acknowledgements

# Chapter 1

# The NA44 Experiment

## 1.1 The General Concept

In the design of fixed target heavy ion experiments, one can distinguish two opposite stratagems:

- Emphasise quality of a given set of measurements (resolution, cleanliness of particle identification). Sacrifice broadness of scope in order to fully concentrate on the selected measurements.

- Emphasise broadness of scope (acceptance, variety of identifiable particles). Sacrifice quality of measurements (resolution, quality of particle identification).

A clear awareness of one's stratagem, readiness to counteract its drawbacks and fully utilize its strengths is an essential prerequisite of success. The choice of a stratagem (or, in a mixed case, choice of a proportion of the mix) is driven by the experiment's goals. The goals of the NA44 Experiment have been:

- Handbury-Brown–Twiss (for short, HBT) interferometry with pions, kaons and protons, reaching a formulation as complex as 3D.

- Single particle spectra of pions, kaons, protons, antiprotons, deuterons, antidueterons, and even tritons. In particular, a study of low $p_T$ features of the spectra around midrapidity.

- Measurements of the abundances of the above mentioned particles.

Thus ordered, the goals entail the design concept of an experiment, which follows the first stratagem: *a focusing spectrometer*. Focusing magnetic field provides for excellent momentum resolution, but can be effective only in a narrow region of phase space. Hence the smallness of track multiplicity that enables clean particle identification using the relatively simple techniques based on the time-of-flight and the Cherenkov radiation.

## 1.2 Target

In the $Pb$ run, we used $Pb$ targets made in shape of a 1cm diameter disk of 1.15 or 2.3 $g/cm^2$ thickness. Interaction probability in the target can be estimated, scaling the known [1] nuclear inelastic cross-section ($\sigma(pPb) = 1.77 barn$) in proportion to the number of primary collisions between individual

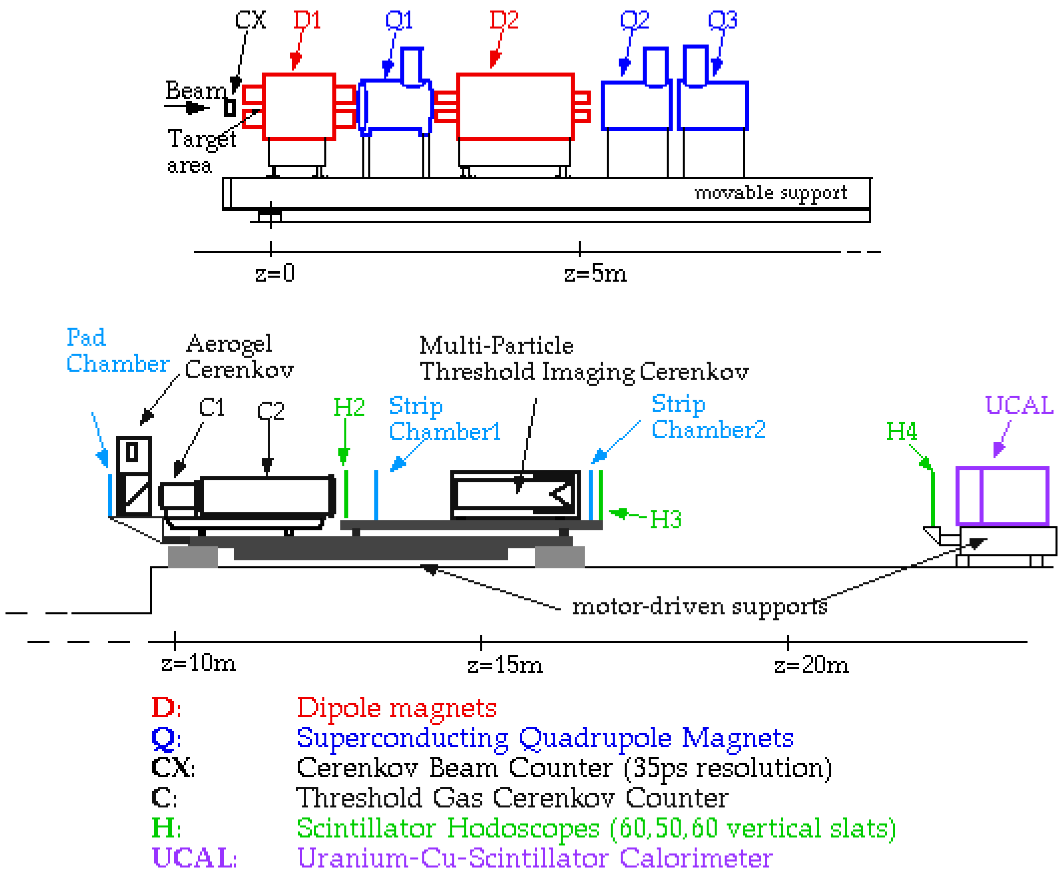


Figure 1.1: The NA44 spectrometer during the Pb beam running.

participants (1 for $p$, 208 for $Pb$): [1]

$$\frac{\sigma(PbPb)}{\sigma(pPb)} = \left(\frac{2 \times 208^{\frac{1}{3}}}{1^{\frac{1}{3}} + 208^{\frac{1}{3}}}\right)^2 \approx 2.93 \qquad (1.1)$$

When the interaction cross-section $\sigma$ is known, the interaction probability is $\sigma N_A d/\mu$, where $d$ is target thickness in $g/cm^2$, $N_A$ is the Avogadro's number, and $\mu$ is molar mass of the material in $g/mol$. For the two target thicknesses mentioned, the interaction probabilities would be, respectively, 1.7 and 3.4 %.

## 1.3 Trigger

The art of experiment is to make the equipment answer as accurately as possible the questions we ask, while being as insensitive as possible to what we deem irrelevant. Ability to feel the difference between what can be made irrelevant and what can not depends on the knowledge previously acquired, and is among the experimentalist's most precious qualifications. The purpose of a trigger is to allow the experiment to focus its attention on the selected topic. In this focusing of attention, important is a controlled graduality of stages. For this reason, an hierarchy of trigger conditions is maintained. In its turn, the hardware *trigger* (i.e. the permission to record the information from the equipment) itself forms the preliminary stage for a more complex off-line analysis. Its negative consequences can not be overcome off-line, but

[1]With the normalization technique actually used, the accuracy of this estimate does not affect the accuracy of the normalized particle yields, and the estimate is given here for orientation only.

can only be corrected for, in which process the richness and complexity of the above-mentioned hierarchy plays the crucial role.

How important is the issue of a trigger ? An accelerator delivers spills of particles with given momentum to the target. A typical duration of a spill is about 5 s, during which about $4 \times 10^6$ particles cross the target. A typical NA44 run used for single particle analysis lasts for about 100 spills, and records a tape with about $4 \times 10^4$ events. Having an interaction in the target is therefore roughly two orders of magnitude more frequent an event than writing a selected event to the tape. This means that by virtue of the NA44 trigger, these $4 \times 10^4$ events can be easily collected so that each of them contains a proton or a kaon, or a pion pair, or at least one charged particle of any identity. With some change in the numbers, but without difficulty, samples of kaon and proton pairs for correlation analysis can be obtained. This section explains how this is possible.

### 1.3.1 Valid beam condition ($VB$) and beam counting

A gaseous Cherenkov beam counter [2] and a geometrical veto scintillation counter provide a positive indication of a beam particle's passage through the target. This indication constitutes the simplest possible form of an NA44 trigger, known as the *valid beam trigger*. The beam counter provides a 35 ps accurate start time reference for subsequent time of flight measurements via scintillating hodoscopes (see section 1.6.1). The beam count, provided by this detector, is needed to convert particle counts in the spectrometer into average particle yield for a given event centrality.

### 1.3.2 Trigger detector of charged particle multiplicity (*T0*)

To characterize event multiplicity and to implement multiplicity trigger, NA44 has a plastic scintillator counter positioned 3 cm downstream of the target and known as T0. It consists of two parts, each in shape of a rectangular parallelepiped $3 \times 12 \times 15$ mm, placed symmetrically around a vertical plane passing trough the center of the target, with a 3 mm gap between them. T0 covers $1.4 \leq \eta \leq 3.7$ for an $\eta$-dependent fraction of azimuthal angle, $0.22 \leq \Delta\phi/2\pi \leq 0.84$ respectively. Each half of the detector is equipped with two photomultiplier tubes (PMTs) for optical readout of scintillations. Signals from both halves of T0 are required to pass a discriminator threshold to form a *centrality trigger*. Normally, the discriminator thresholds were set so that the probability of a centrality trigger for an interaction event did not exceed 15%.

### 1.3.3 Multiplicity trigger (*MUL1*)

It may happen that even though the T0 centrality trigger is present, the spectrometer (primarily due to the azimuthal narrowness of its acceptance) gets no reconstructable tracks, and the event is of no use for the analysis. In the Pb beam period, the tracking device of the limiting acceptance was the pad chamber, which replaced the H1 hodoscope. For this reason, since 1995, we required a hit in the pad chamber along with at least one hit slat in each of the scintillation hodoscopes H2 and H3 ($MUL1 \cdot PC$). To analyse correlations among identical particles, NA44 triggered on double track multiplicity. In this work, by *multiplicity trigger* a requirement of at least a *single* track is always meant.

### 1.3.4 Cherenkov veto trigger ($\bar{C}1 \cdot \bar{C}2$ and $\bar{C}2$)

Experience shows that at high energy nucleon collisions, majority of emitted particles are pions. In NA44, the product of the valid beam, centrality and multiplicity triggers provides a sample of events, strongly dominated by single pions. Measurements of kaons and protons, especially the HBT-correlation studies, require a dedicated trigger. It is implemented by vetoing events with noticeable emission of Cherenkov light in the medium with specially selected refraction index. By vetoing such events, one is able to get rid of the light particles, because

1. the Cherenkov photons of frequency $\omega$ are emitted by the medium when the charged particle's velocity $v$ exceeds the phase velocity of electromagnetic waves with frequency $\omega$ in that medium: $v > c/n(\omega)$, where $n(\omega)$ is the refraction index;

2. momenta of the different particles in the detector's acceptance are made nearly equal by the spectrometer optics, so that the differences in the velocity arise solely because of the particle mass.

| Detector | Pressure, atm. | $e$ | $\pi$ | $K$ | p |
|---|---|---|---|---|---|
| $C1$ | 2.7 | 0.0 | 1.8 | 6.4 | 12.1 |
| $C2$ | 1.3 | 0.0 | 5.2 | 18.3 | 34.8 |

Table 1.1: Threshold momenta (GeV/c) of common charged particles for $C1$ and $C2$.

| $< p >$ GeV/c | $< (p - < p >)^2 >^{\frac{1}{2}}$ GeV/c | function in the trigger | | Trigger mode |
|---|---|---|---|---|
| | | $C1$ | $C2$ | |
| 4.1 | 0.4 | ignored | ignored | no Cherenkov bias |
| 4.1 | 0.4 | veto | veto | $\pi/e$ veto |
| 7.7 | 0.6 | ignored | ignored | no Cherenkov bias |
| 7.8 | 0.7 | ignored | veto | $\pi/e$ veto |

Table 1.2: Functions of the Cherenkov detectors in the trigger for various momentum settings

NA44 has two Cherenkov threshold detectors, known as $C1$ and $C2$. The information on their thresholds and functions in the trigger, collected in tables 1.1 and 1.2, illustrates their use.

### 1.3.5 Use of the trigger modes

The data points for published single particle distributions come from the $VB \cdot T0 \cdot PC \cdot MUL1$ trigger mode, complimented in case of Cherenkov veto by either $\bar{C}1 \cdot \bar{C}2$ or $\bar{C}2$ for collection of $K/p$ samples (see subsection 1.3.4). For each setting of the spectrometer's angle and magnetic field, the data was taken with and without the Cherenkov veto, to understand the effect of the latter. $VB \cdot T0$ and $VB \cdot PC \cdot MULT1$ data is instrumental in understanding the effect of $T0$ and $PC \cdot MULT1$ on the multiplicity of the sample.

## 1.4 The Si pad detector

The Si pad array, installed 10cm downstream from the target, measures ionization energy loss of charged particles ($dE/dx$) in its 512 300 $\mu$m thick Si pads covering $1.5 \leq \eta \leq 3.3$ and $2\pi$ azimuthally. Radially, the pads are arranged to be fragments of 16 rings with equal pseudorapidity coverage (see Fig.1.2 ). Azimuthally, they constitute 32 sectors with equal angular coverage. $\delta$-electrons, produced by the $Pb$ nuclei of the beam especially copiously in the target, are swept away to one side by the magnetic field of the first dipole ($\approx$ $1.6Tl$ in the strong field setting). Because the energy spectrum of $\delta$-electrons is dominated by low energies, this sweeping effect of the field leaves the other half relatively clean and useful for multiplicity analysis. The amplitudes are read out by AMPLEX [3] and digitized by DRAMS [4]. By *occupancy* $\mu$ of a Si pad we will mean the average number of hitting tracks:

$$\mu = \sum_{i=0}^{\infty} w_i i, \tag{1.2}$$

where $w_i$ is probability of having $i$ hits in the pad. Typically, in the central trigger runs, the occupancy is somewhat above 1. [2]

Relation of the detector/electronics time characteristics to the interaction frequency was safe with respect to pile-up by a large margin. [3]

The data from the detector was used in the texture analysis of the hadron production (using the data recorded in 1994), and in the analysis of meson production in the $Pb$+$Pb$ collisions to normalize particle yields (the 1995 data). In the latter case, the same detector was used in its second running period, so that radiation damage was noticeable. In both cases, more information on the detector and its characteristics will be given in the appropriate sections.

---

[2] An estimate for orientation: for Poissonian distribution of hits, $\mu = 1$ means that probability of having 1 or more hits is $1 - P(0) = 1 - exp(-1) \approx 0.63$, i.e. the detector, in fact, is merely semi-occupied.

[3] The charge collection time for a 300 $\mu m$ path length in the Si is typically 10-20 ns [6]. AMPLEX has 600 to 800 ns signal processing time [3]. Duration of an SPS spill was about 4.7 s, the NA44 was typically operating at (2-4)$\times 10^6$ beam particles per spill. The thickest Pb target used had 0.034 interaction probability for the Pb beam. This means that the typical rate of minimum bias interactions was always below 31 kHz, i.e. on average 32 $\mu s$ per interaction, and pile-up was impossible.

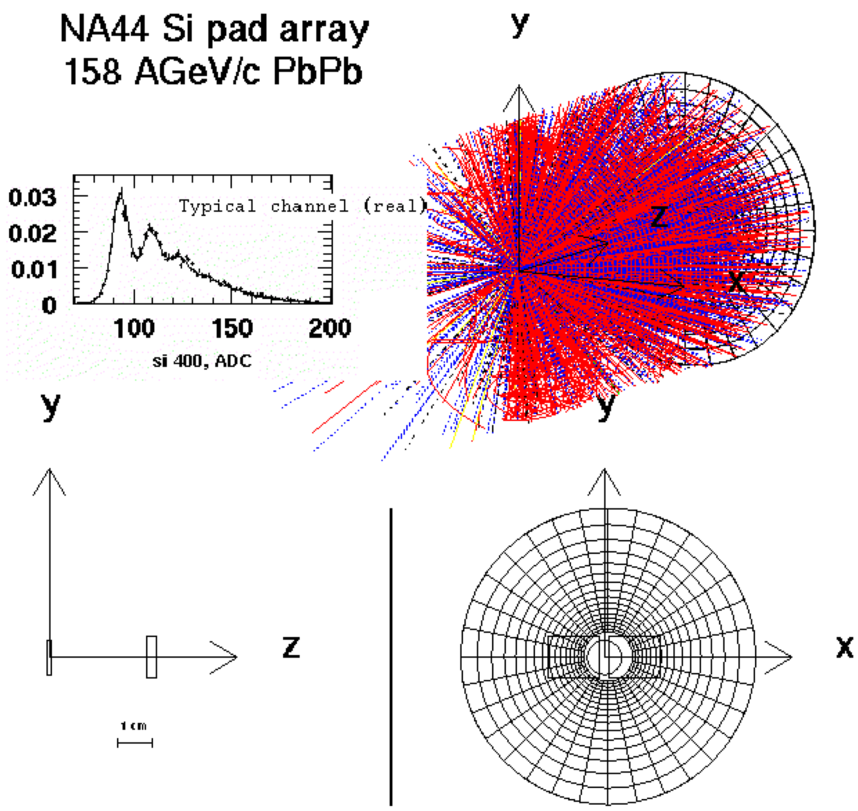


Figure 1.2: NA44 multiplicity detector complex: Si pad array (shown with the actual geometrical XY offset, found by off-line analysis) and T0 scintillators. The tracks are from a simulated RQMD Pb+Pb event. Also shown is an ADC distribution from a typical Si channel.

## 1.5 Spectrometer "optics". Acceptance.

A magnet system of two dipoles and three superconductive focusing quadrupoles, together with a tracking complex (a pad chamber, three highly segmented scintillation hodoscopes H2, H3, H4 and two strip chambers, see Fig.1.1) provides momentum resolution of 0.2% or better for all spectrometer settings. The quadrupoles allow for two modes of focusing – vertical and horizontal. The distinction between them plays a role in HBT analysis; in the single particle analysis the horizontal mode has always been used. The spectrometer accepts charged particles of a single charge at a time. The magnet system is mounted on a rotating platform and was operated at two angular positions (44 and 131 mrad). The data analyzed are taken with two different field strengths. In the weak field mode, spectrometer accepts charged tracks in the momentum range of $3.3 < p < 5.1$ GeV/$c$, and of $6.3 < p < 9.7$ GeV/$c$ in the strong field mode. These two field modes are often called "the 4 GeV/c" and "the 8 GeV/c" settings, respectively. Location of the acceptance area in rapidity $y$ and transverse momentum $p_T$ varies with field strength, arm angle, and particle mass, as is shown on Fig. 1.3. For $K$ and $\pi$, the acceptances are located within one unit of $y$ around the center-of-mass rapidity of the SPS $PbPb$ system ($y_{CM} = 2.92$) [4]. The magnitude of the spectrometer's acceptance is largely restricted by the factor $\Delta\phi/2\pi$ (typically around 0.02) representing

[4]Their peculiar "banana" shape in the $p_T$ and $y$ variables is due to the constraint, imposed on $p_T$ and $p_z$ by constancy of momentum $p$ : ${p_T}^2 + {p_z}^2 = p^2 = const$, and, differentiating, from $dp/\,dy = 0$ one gets $dp_T/\,dy = -p_z E/p_T < 0$.

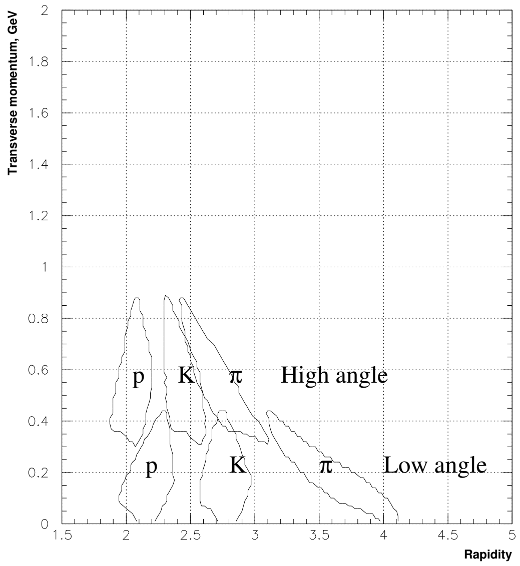


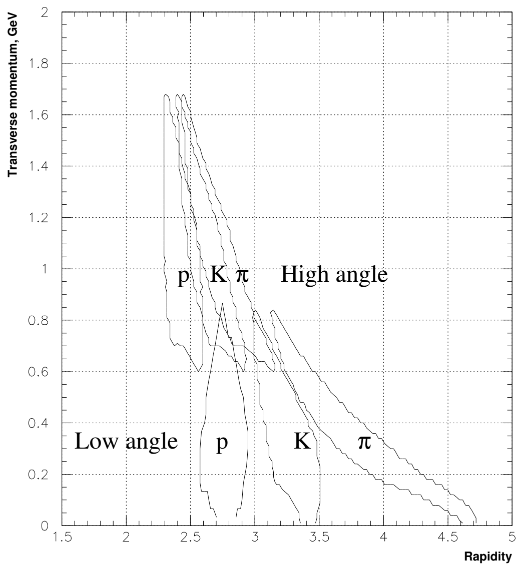


Figure 1.3: Acceptance area of the NA44 spectrometer in the laboratory rapidity $y$ and transverse momentum $p_T$. Top: in the weak field mode; bottom: in the strong field mode.

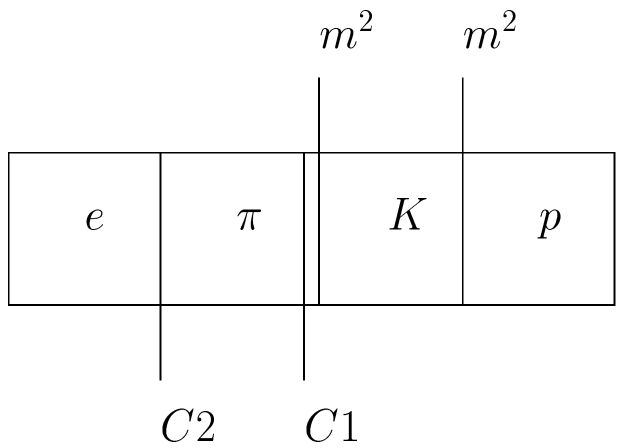


Figure 1.4: Means of particle identification in the weak field settings

narrowness of the azimuthal coverage. Within the spectrometer's acceptance at $p_T = 0.4$ GeV/c for a midrapidity pion, the remaining factors would amount to about 0.5. In the low angle setting during the $Pb$ run, a tungsten collimator (the so called "jaws") was introduced into the magnet system in order to reduce the multiplicity of tracks in the spectrometer. Its effect on the acceptance has been computed via Monte Carlo and corrected for in the analysis. More detailed discussion of these issues will be given in the Analysis chapter.

## 1.6 Means of particle identification

### 1.6.1 Tracking and time of flight

Three highly segmented scintillating hodoscopes (H2, H3 [7], H4) and three multiwire proportional chambers (MWPC) with cathode-segment readout (a pad chamber, PC, and two strip chambers, SC1 and SC2, each having

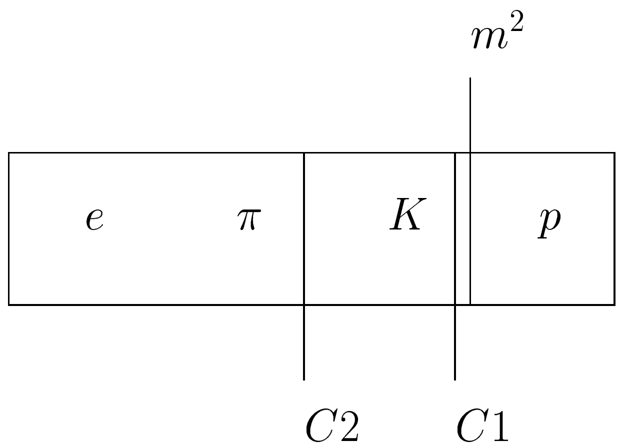


Figure 1.5: Means of particle identification in the strong field settings

a plane of vertical and a plane of horizontal strips) form the tracking system [5] (see Fig. 1.1). In NA44, magnets and tracking detectors are separated in space so that tracks of charged particles are straight. There is no trackers in the target area before the magnets.

Time of flight measurements with accuracy not worse than 100 ps are performed via H2, H3 [7], with the Cherenkov beam counter (described above in section 1.3.1) being the source of the start time reference with 35 ps accuracy. The hodoscopes are segmented along the momentum-sensitive coordinate (i.e. horizontally) into vertical slats, sufficiently narrow so as to be able to detect particle pairs with momentum difference of $50 MeV/c$ at $p = 10 GeV/c$ in different slats. The scintillation light is read out from top and bottom of each slat by two PMTs, so that sensitivity to the vertical coordinate is gained from the comparison (though rendered obsolete with the addition of the strip chambers

[5] With '94 and '95 data, H4 was not yet used in the offline analysis.

for the $Pb$ running).

The NA44 MWPCs measure ionization energy losses of charged particles in the 50%/50% $Ar/C_2H_6$ gas mixture. Primary ionization is "amplified" in the process of avalanche ionization in the highly non-linear electrostatic field near the 20 $\mu m$ anode wire. A cloud of charge, drifting under the influence of field, induces electrical pulses on the electrodes. The cathode is split into rectangular pieces, read out by separate channels of AMPLEX [3] chips. Normally, the same avalanche results in measurable inductions on several (4-8) channels, so that one can talk, in a sense, of an "image" of the avalanche, reconstructable off-line with good resolution: the required RMS of 2-3 hundred $\mu m$ along the direction of the anode wire has been easily achieved. More details about NA44's MWPCs are found in [8].

### 1.6.2 The Cherenkov's counters

The use of Cherenkov's counters for particle identification and the principles of their operation have already been described in section 1.3.4. More information on the inefficiencies associated with the Cherenkov vetoing will be given in sections 2.4 and 2.5.

### 1.6.3 The Uranium Calorimeter (UCAL)

NA44 uses nine stacks of a fine-sampling Uranium/Copper/scintillator Calorimeter with wavelength shifter readout, originally designed [5] for the AFS experiment at ISR. Each stack is sub-divided into six towers. Each tower has two sections, read out separately: a 6 radiation lengths ($6X_0$) long electromagnetic one, and a 3.8 absorption lengths ($3.8\lambda_I$) long hadronic absorber. Each section is read out by two PMTs collecting light from two light guides that cover left and right flanks of the section. [6] Two characteristic features of this device are

- nearly identical response to charged and neutral pions [7] (not required by NA44)
- self-calibration by measuring fission signal.

NA44 uses UCAL for $e/\pi$ separation. In particular, in this analysis UCAL was used to determine how many pions are lost due to the Cherenkov electron veto in the trigger (see subsection 2.4.3). This is possible due to the longitudinal separation of the tower into electromagnetic and hadronic sections. The electromagnetic showers tend to have a predominant contribution from the electromagnetic section. Due to the low track multiplicity in the spectrometer, the UCAL's granularity is sufficient to associate tracks with towers.

---

[6] By mid 1990s, after the long years of service, the scintillator's transparency became reduced by radiation damage to a level which severely undermined independence of the signal on the impact position along the face of the stack. I had to correct for that problem – more on this in section 2.4.

[7] In UCAL, 1-10 MeV neutrons from the nuclear break-ups in hadronic showers do not go unnoticed but induce fissions. These fissions contribute to the measured signal, thus rising it to a level typical for an electromagnetic cascade caused by decay products of a $\pi^0$ of the same energy.

# Chapter 2

# Technique of the NA44 single particle analysis

In this chapter I discuss the problems of the off-line data analysis: acceptance correction, trigger centrality determination, cleanliness and efficiency of particle identification, and conclude with a summary review of sources of systematic errors to the single particle yields and distributions. Preliminary discussion of particle identification is found in section 1.6.

## 2.1 Acceptance correction

I start with acceptance correction because this is a problem whose solution does not depend on the information presented in the rest of this chapter. On the other hand, a procedure to determine the trigger centrality, reported in section 2.2, involves an acceptance correction.

### 2.1.1 Introduction and definitions

The total energy $E$ and a three-dimensional vector of momentum $\vec{p}$ of a particle, emitted in an interaction, along with that particle's internal quantum numbers (mass $m$, charge, spin, strangeness, baryon number, etc), carry important information about dynamics of the interaction. The simplest way to analyze this information is by using statistical distributions of particles with respect to various kinematical variables, derived from its Minkovsky energy-momentum four-vector $(E, \vec{p})$. Among such variables are

- transverse momentum $p_T = \sqrt{p_x^2 + p_y^2}$,
- transverse energy $m_T = \sqrt{p_T^2 + m^2}$,
- transverse kinetic energy $k_T = m_T - m$,
- rapidity $y = 1/2 \ln((E + p_z)/(E - p_z))$,
- pseudorapidity $\eta = -ln(tan(\theta/2))$, where $\theta$ is zenith angle.

It is a popular practice to use $m$, $p_T$, $y$ and azimuthal angle $\phi$ instead of $(E, \vec{p})$, because in the former set of variables three $(m, p_T, \phi)$ are Lorentz-invariant with respect to translations along the $z$ axis, whereas $y$ is Lorentz-transformed by a simple addition of a number, so that $\Delta y$ is Lorentz-invariant.

In particle physics, one uses the notion of a differential cross-section of particle production [1]

$$\frac{E\, d^3\sigma}{dp^3} \tag{2.1}$$

With our preferred set of kinematical variables, one notices that

$$\frac{E\, d^3\sigma}{dp^3} = \frac{E\, d^3\sigma}{d\phi p_T\, dp_T\, dp_z} = \frac{d^3\sigma}{d\phi p_T\, dp_T\, dy} = \frac{d^3\sigma}{d\phi m_T\, dm_T\, dy} \tag{2.2}$$

Whatever reference is chosen to measure $\phi$, in practice one will see a set of interaction events averaged over all possible azimuthal orientations of the colliding system, unless one's experiment is more sensitive to some of them than to others. For experiments which do not distingush azimuthal orientations (like NA44), the nature performs a Monte-Carlo integration of Eq. 2.1 over $\phi$, and one is left with

$$\frac{d^2\sigma}{m_T\, dm_T\, dy}. \tag{2.3}$$

It may be more direct to talk about

$$\frac{d^2 N}{m_T\, dm_T\, dy}, \tag{2.4}$$

[1]The reason to choose *this* Lorentz-invariant combination of quantities is the fact that differential cross-section of an interaction of particles $A$ and $B$ with an arbitrary number of secondaries (indexed by $f$) in the final state is given by [9]

$$d\sigma = ((2S_A+1)(2S_B+1)4j)^{-1} \times \sum_{S_i,S_f} |M|^2 (\prod_f \frac{dp_f{}^3}{2E_f(2\pi)^3})(2\pi)^4 \delta^4(p_A+p_B-\sum_f p_f)$$

where $j$ is an invariant flux, $S_A$, $S_B$, $S_f$ are spin quantum numbers, and $|M|^2$ is the squared modulus of the invariant amplitude of the process. Therefore Eq. 2.1 represents the $|M|^2$ integrated over the phase space of the non-observed particles, with certain coefficients.

$N$ being the number of particles of given identity emitted in an interaction event. What one measures however is

$$\frac{d^2n}{m_T\,dm_T\,dy} = A(y,m_T)\frac{d^2N}{m_T\,dm_T\,dy}, \tag{2.5}$$

where $A(y,m_T)$ is an *acceptance function.* $A(y,m_T) < 1$ due to experimental inefficiencies. Technically, $A(y,m_T)$ is represented in the analysis by a Monte Carlo simulation procedure and takes into account the effects of focusing and analyzing optics as well as tracking efficiency and decays:

$$MC_{output} = MC_{input}A(y,m_T) \tag{2.6}$$

The output from the single particle analysis will be presented in form of 1D distributions, or integrals of Eq. 2.4:

$$\frac{dN}{dy} = \int_m^\infty \frac{d^2N}{dy\,dm_T}\,dm_T, \quad \frac{dN}{m_T\,dm_T} = \int_{y_{min}}^{y_{max}} \frac{d^2N}{dym_T\,dm_T}\,dy \tag{2.7}$$

### 2.1.2 How to extract the one-dimensional distributions

Acceptance of the NA44 spectrometer is discussed in section 1.5 and presented on Fig. 1.3. In determining $dN/\,dy$ and $dN/m_T\,dm_T$ for kaons and pions we use spectrometer settings, or portions thereof, with $\Delta y = 0.2 - 0.6$. The slope parameter(s) do not depend appreciably on $y$ within this small range. [2] Then the double differential multiplicity can be factorized [3] as

$$\frac{d^2N}{dy\,dm_T} = B(y)T(m_T) \tag{2.8}$$

In parallel to the equations (2.7), for the observable particle counts one can define

$$\frac{dn}{dy} = \int_m^\infty \frac{d^2n}{dy\,dm_T}\,dm_T \tag{2.9}$$

$$\frac{dn}{dm_T} = \int_{y_{min}}^{y_{max}} \frac{d^2n}{dy\,dm_T}\,dy \tag{2.10}$$

(Technically speaking, they are projections of 2D histograms.) Integration of Eq. 2.5 assuming that Eq. 2.8 holds yields

$$\frac{dn}{dy} = B(y)\int_m^\infty T(m_T)A(y,m_T)\,dm_T \tag{2.11}$$

If Eq. 2.8 is true, $dN/\,dy$ from Eq. 2.7 can be rewritten as

$$\frac{dN}{dy} = B(y)\int_m^\infty T(m_T)\,dm_T \tag{2.12}$$

Eliminating $B(y)$, we conclude the "theoretical justification" for what is known as a 1D acceptance correction:

$$\frac{dN}{dy} = \frac{dn}{dy}\frac{\int_m^\infty T(m_T)\,dm_T}{\int_m^\infty T(m_T)A(y,m_T)\,dm_T} \tag{2.13}$$

---

[2] This is supported by the existing data [10] on the change of $< p_T >$ with $y$ for primary negative hadrons. As $y$ goes from 3.4 to 3.9, $< p_T >$ drops from $\approx 0.382$ $GeV/c$ to $\approx 0.378$ $GeV/c$, i.e. by $\approx 1\%$. Such an effect is likely to be suppressed by other error bars.

[3] $B(y)$ and $T(m_T)$ are defined by Eq. 2.8 itself. Either one of them therefore can contain an arbitrary multiplier. For our goals, this ambiguity is irrelevant, as will be clear from the way $B(y)$ and $T(m_T)$ enter Eq. 2.13 and Eq. 2.14.

Similarly, for the $m_T$ spectrum we get

$$\frac{dN}{dm_T} = \frac{dn}{dm_T} \frac{\int_{y_{min}}^{y_{max}} B(y)\, dy}{\int_{y_{min}}^{y_{max}} B(y) A(y, m_T)\, dy} \tag{2.14}$$

Similar equations can be obtained for $p_T$ or $k_T$. In principle, one needs to know $B(y)$ and $T(m_T)$ in order to determine the true shape of $m_T$ spectrum and $dN/\,dy$. In practice, for pions $B(y)$ was taken to be a Gaussian with $\sigma = 1.4$ [4] centered at mid-rapidity; for kaons – a Gaussian with $\sigma = 1.1$. [5] For the acceptance correction in $y$, I used

$$1/m_T\, dN/\, dm_T = \sum_{i=1}^{8} w_i \exp(-m_T/T_i) \tag{2.15}$$

Here $w_i$ are 8 variable parameters, $T_i$ are fixed "temperatures". For pions, all 8 parameters were used; for kaons, good fits could be obtained with only one $T$ parameter (see Table 3.1).

### 2.1.3 Corrections for the inefficient hodoscope slats

Some slats of H2 and H3 have had no signal part of the time. A Monte Carlo inefficiency correction procedure [6] was used to correct for that. It was

[4] This is the $\sigma$ of the pion distribution according to RQMD and also the $\sigma$ of the NA49's $h^-$ [10] distribution. My attempts to determine this parameter from our own pion data led me to conclude that this can only be done with accuracy as poor as 50% because of narrowness of our coverage in $y$. The result however is consistent with NA49 and RQMD. This remark applies to the kaons too.

[5] As in RQMD.

[6] due to Michael Murray

based on efficiency monitoring carried out off-line run-by-run. The efficiency of suspect channels in a particular run was calculated by comparison of its bin content with two neighboring ones. Number of tracks in a run would be recorded. The overall efficiency of a channel throughout a series of runs used in the analysis would be calculated as a weighted average efficiency. The total loss of efficiency due to the slat malfuction was of the order of few percent.

### 2.1.4 Acceptance correction for the non-identified tracks

In the task of finding the centrality of the physics trigger settings (discussed in section 2.2), the problem of obtaining $dN/d\eta$ of the spectrometer for comparison with the Si pad array arose. Technically, the solution was facilitated by the (quite artificial !) trick of assigning a pion mass to every particle regardless of its identity, then fitting the so obtained "$k_T$" distribution by the multitemperature formula 2.15 and extrapolating [7] for every setting from $p_T = 0$ to $p_T = \infty$ to get $dN/d\eta$.

### 2.1.5 Imperfections of the acceptance correction and the effects thereof

Due to inaccuracies of our knowledge of the geometrical positions of the equipment in the hall and of the magnitude and configuration of the magnetic

[7] here the artificial mass assignment is equivalent to changing the integration variable within the integral and does not change the result

field, the acceptance correction is imperfect. It is less reliable on the edges. Typically, when looking at either $dN/dy$ or $k_T$ spectra from a single setting with sufficiently fine binning one sees points on the edges of acceptance that deviate sharply from the overall pattern. These points must be dropped. [8] A sharp non-constancy of $dN/dy$, inconsistent between different settings, would indicate that a wrong $T(m_T)$ was used.

Acceptance correction to the $m_T$ or $p_T$ spectra includes information about shape of the $dN/dy$ distribution. Therefore any uncertainty in the $dN/dy$ shape results in an uncertainty of the slope. In quantifying the uncertainty, the first step was to derive the error propagation factor to convert the uncertainty of the $dN/dy$ width into uncertainty of the inverse slope $T$. MC was run with two widths of input $dN/dy$: $\sigma_1 = 1.1$ and $\sigma_2 = 0.5$. The slopes were extracted in the two cases and compared, the error-propagation factor was found to be [9]

$$dT/d\sigma = (T(\sigma_1) - T(\sigma_2))/(\sigma_1 - \sigma_2)$$

It is : for 8 GeV/c high angle: $-52MeV/(\text{unit of }\sigma)$, for 4 GeV/c high angle: $-117MeV/(\text{unit of }\sigma)$. The problem however is to characterize the uncertainty of our knowledge of the $\sigma$. This has been done in the following (somewhat arbitrary !) way: I say that with "$3\sigma$" (99.7%) confidence level, the Gaussian

---

[8] The resulting $y$ ranges are listed in Table 3.2.

[9] assuming that the dependence of the apparent inverse slope $T$ on the width is smooth enough so that it can be inter- and extrapolated by the two points.

kaon $dN/dy$ distribution has $\sigma$ parameter between 0.8 and 1.4. [10] Then, one can derive and propagate the "$1\sigma$" uncertainty. The resulting uncertainty in the inverse slope can be found in Table 3.1.

## 2.2 Determination of the trigger centrality

In NA44, the trigger-level centrality selection combines T0 multiplicity discrimination with the inherent centrality-biasing effect of the narrow midrapidity acceptance of the spectrometer. Sophistication of the normalization issues is therefore a natural conceptual feature of the experiment. In the present work, centralities of the physics settings were determined from 1995 data using the Si pad array *multiplicity*, via a method developed by the author to respond to the specific challenges of this particular experiment and a particular data set. In this method, the trigger centralities play the rôle of "calibration constants" that ensure consistency of the absolutely normalized spectrometer and Si data. Apart from the normalization factors themselves, this section provides justification of the method and gives reasonable amount of technical background information.

### 2.2.1 The problem of absolute normalization

The problem of absolute normalization arises when one wants to obtain the event averaged number of particles $\langle N \rangle$ emitted in the collision events of

---

[10] The somewhat arbitrarily chosen number here is 99.7%.

certain centrality (impact parameter) range, or probability density distributions of particle emission with respect to kinematical variables.

$$N = \frac{n}{E}\frac{1}{\mathcal{A}}, \tag{2.16}$$

where the desired average $N$ is calculated from the number $n$ of detected particle tracks over $E$ collision events of given trigger-selected class, using the apparatus which registers only $\mathcal{A} \leq 1$ fraction of such tracks.

$$E = B \times i \times c, \tag{2.17}$$

where the $E$ collisions are selected from the $B \times i$ inelastic beam-target interactions by means of the trigger. The trigger is represented by quantity $c$, which will be called trigger centrality. The interaction probability $i$ in eq. ( 2.17) is not measured precisely. Unknown in the eq. ( 2.17 ) is $i \times c$. The beam count $B$ is measured by the Cherenkov beam counter (section 1.3.1, [2]). In this section I quote $c$, assuming that $i = 0.034$ (as discussed in section 1.2).

The $E$ includes collisions with and without tracks in the acceptance. Important here is that even though the $E$ includes collisions with no tracks in the acceptance, the requirement for them to be of the same centrality class as the trigger events (to ensure "cleanliness" of the average (2.16)) forces one to pay attention to all centrality-sensitive components of the trigger. The notion of the **trigger-selected centrality class**, or sample, and its characteristic $c$ becomes therefore the key issue of the normalization analysis.

$c$ is the fraction of inelastic interactions, which includes all of the following and only the following:

**(a)** interactions that satisfy the trigger requirements

**(b)** for every interaction of group (a), all interactions of the same *total multiplicity* that happened in reality during the run, but did not cause triggering due to absence of tracks in the spectrometer's acceptance, and only due to this reason.

In this text, the class of events just described will be also referred to as the "normalization sample" or "$c$-sample". This definition of $c$ guarantees that the $N$ in formula (2.16) is indeed the correct average multiplicity in the centrality class selected by the trigger.

One should bear in mind that there is also a group of events which *do not* belong to the same total multiplicity class as the trigger events, have *acceptable* T0 amplitude in the trigger and do not create tracks in the spectrometer. They must be excluded from the definition of the trigger-selected centrality class and be not confused with the events of group (b) ! (Otherwise the result will be an underestimate of the true $N$ !). This subtlety would not exist for a large acceptance experiment, due to absence of the group (b) itself. Among the mechanisms responsible for existence of the events with lower total multiplicity but acceptable T0 amplitude are $\delta$-electrons, noise and fluctuations associated with operation of T0, fluctuations in the distribution of charged tracks in space.

Let us list the centrality-sensitive components of the trigger and briefly discuss them.

### 2.2.2 Rôle of T0

The fraction of the full azimuthal angle covered by T0 depends on the (pseudo)rapidity and varies between 0.84 for $\eta = 3.7$ and 0.22 for $\eta = 1.4$, being 0 outside this $\eta$-range. Due to geometrical reasons, a "natural" (no trigger bias) sample of collisions is dominated by peripheral ones. To what extent do the peripheral collisions with pronounced reaction plane (and fragmentation ?) effects "emulate" the T0 response typical for the central events, given the mirror-symmetric (rather than azimuthally symmetric) geometry of T0 ? Our analysis of the Si pad array multiplicity allows to say that the combination of T0 discrimination with the "midrapidity" trigger coming from the spectrometer (*MUL1*) selects a fairly homogeneous sample of events without exceptionally low Si multiplicities. In the normalization scheme being described, the T0 amplitude of the $\delta$-free side (and only it) is used to define samples of different centralities.

### 2.2.3 Rôle of *MUL1*

Distribution of the number of tracks that hit the spectrometer's acceptance deviates from the Poissonian one due to two-particle and multiparticle correlations. Realizing that, it is nevertheless useful to recall that in the Poissonian case with average $\mu$, $(n+1)P(n+1)/P(n) = \mu$. Upon comparison with the ratio of double to single track events we see in the central trigger runs of our experiment, it is clear that even in Pb+Pb, the spectrometer (even in the low angle setting, due to the "jaws") presents a target which is difficult to hit

($\mu \ll 1$). I use

$$P(0) \simeq \exp(-2P(2)/P(1)) \tag{2.18}$$

as a measure of the probability that the spectrometer has zero tracks. (In case of the Poissonian law, the equation (2.18) would be exact. The current discussion however does not pursue more than qualitative understanding.) Table 2.2.3 summarizes the Poissonian estimates of $P(0)$.

| momentum | + 4 GeV | | + 8 GeV | | - 4 GeV | | - 8 GeV | |
|---|---|---|---|---|---|---|---|---|
| $p_T$ setting | low | high | low | high | low | high | low | high |
| $h$ | 0.76 | 0.91 | 0.71 | 0.95 | 0.77 | 0.92 | 0.72 | 0.96 |
| $K/p$ | 0.96 | 0.97 | 0.93 | 0.97 | $h^-$ | 0.99 | 0.97 | 0.99 |

Table 2.1: The estimated fraction of events that do not create tracks in the spectrometer. It has been obtained according to the Poissonian law, $P(0) \simeq \exp(-2P(2)/P(1)$, based on the DST information.

Had it been easy to satisfy ($\mu \geq 1$), the *MUL1* requirement would not have been considered important component of the centrality trigger. Therefore, *MUL1* needs to be taken into account for determination of the trigger centralities.

### 2.2.4 General idea of the procedure

Based on the discussion in the previous sections, one can foresee two directions that lead to the correct determination of the $c$-sample:

1. direct (or indirect) counting of events that satisfy the set of conditions which makes up the $c$-sample (see the definition in section 2.2.1). In NA44, the criterion of the $c$-sample has no direct hardware implementation. The author invested a lot of effort into attempts to quantify the difference between the $c$-sample and the samples that do have direct hardware implementation (various trigger modes), by analyzing properties of the latter (e.g., correlations between the amplitudes of left and right T0 scintillators). Dissatisfaction with this path of analysis eventually led me to prefer the following idea:

2. there is a device that does not need the operation of average (as in equation (2.16)) and, therefore, the "normalization sample", to get the multiplicity. The Si pad array measures multiplicity of individual events, event-by-event. For any trigger mode, no matter how complex it is, the Si can give multiplicity of each event taken and thus the average multiplicity. The left-hand side of equation (2.16) becomes known, and so one determines the $c$ of the trigger.

### 2.2.5 How to use the Si pad array

Given the quality of the Si amplitude resolution in 1995, the traditional method of multiplicity analysis, based on the channel-by-channel comparison of amplitude with the MIP expectation, can not be reliably used for the whole run period. Multiplicity analysis can be performed under considerably relaxed requirements to the amplitude resolution, if the probability distribution $P(n)$ of number of tracks $n$, crossing an individual pad of the array, is known. Our eventual goal, sufficient for the task of normalization as it is formulated in the section 2.2.1, is finding a single number, $dN/d\eta$, characterizing the average multiplicity of the whole detector, averaged over all events of a physics run. Therefore it is acceptable to deal with one $P(n)$ for the whole detector, over the whole run (or a set of runs taken with a specific trigger and angular setting). Then, number $H$ of the hit pads ( i.e., pads with signal above the threshold, set during the calibration and subtracted during the DST /footnoteDST – the Data Summary Tape.-production) out of $M$ pads in total, is

$$H = M(1 - P(0)) \tag{2.19}$$

As a measure of Si multiplicity, I use Si occupancy calculated event by event as

$$N = -M \ln(1 - H/M). \tag{2.20}$$

Here $N$ is the number of tracks that cross the array of $M$ channels and create $H$ hits. Equation 2.20 uses the Poisson law for $P(n)$. $N$ is linearly correlated with total amplitude, and for low occupancy cases I use the amplitude (properly calibrated in the units of $N$) instead because in those cases contribution of noise hits (due to drifting pedestals) or absent hits (again due to drifting pedestals) may be significant.

The multiplicity via occupancy expression (Eq. 2.20) has been justified as an integral, or "average", multiplicity over the Si acceptance. Variation of multiplicity from ring to ring is thus neglected. The technical reason for that was the absence of individual ring data in the existing DSTs. If the track density is not uniform over the Si acceptance, the formula results in a systematic error, which will be the larger, the steeper the $dN/d\eta$ is. Let's compare the approximate expression for multiplicity with the exact one.

Approximate (Eq. 2.20 detailed):

$$N = -16M_i \ln(1 - \frac{\sum_{i=1}^{16} H_i}{16M_i}), \tag{2.21}$$

where $M_i$ is number of pads in a ring, $H_i$ is number of hits, and $N$ is the number of tracks crossing the detector.

Exact:

$$N = \sum_{i=1}^{16} N_i \tag{2.22}$$

where every

$$N_i = -M_i \ln(1 - H_i/M_i) \tag{2.23}$$

– from every ring. Therefore the exact formula is

$$N = -M_i \ln(\prod_{i=1}^{16}(1 - H_i/M_i)) \tag{2.24}$$

To summarize, the approximate expression uses the *arithmetic* average in the ln, while the exact one replaces it by the *geometrical* average. We also see that the approximate and exact expression become *identical* if

$$H_1 = H_2 = H_3 = ... = H_{16} \tag{2.25}$$

i.e., if the distribution is uniform over the 16 rings of the detector.

Thus we see that knowledge of the distribution can serve to correct for the systematic error. In principle there are two choices:

- purist: use real Si data to extract the shape of the distribution, and use that information to get the correction.

- pragmatic: we know (and use this knowledge elsewhere in the analysis) that RQMD reproduces the shape of the non-identified charged $dN/d\eta$ fairly well. Use RQMD to get the correction.

I followed the second path. [11] Average number of tracks hitting a pad in a specific ring can be extracted from a properly binned RQMD charged track (+ and −) $dN/d\eta$ distribution:

$$\frac{N}{M} = \frac{\Delta N}{\Delta \eta} \times \frac{\Delta \eta}{M} = \frac{\Delta N}{\Delta \eta} \times \frac{(3.3-1.5)}{16}\frac{1}{32} = 0.0035 \times \frac{\Delta N}{\Delta \eta}$$

because 16 rings (with equal pseudorapidity coverage) of the detector cover pseudorapidity range 1.5 to 3.3, and each ring has 32 pads. Inverting Eq. 2.20, the 16 values of $H_i/M_i$ were obtained – they range between 0.5 and 0.8. Plugging them into the "approximate" and "exact" expressions above yields the correction:

$$\frac{dN/d\eta(exact)}{dN/d\eta(approximate)} = 1.022$$

Conclusion: the multiplier 1.022 needs to be applied to account for deviation of the $dN/d\eta$ distribution from uniformity over the Si acceptance.

[11] In the subsequent event texture analysis, I extracted the $dN/d\eta$ shape from the Si data. It was not different from that of RQMD or HIJING.

### 2.2.6 Si – spectrometer acceptance matching

After the Si multiplicity is obtained, it needs to be compared with the spectrometer $dN/d\eta$. One needs to take into account that Si acceptance is broader and extends further from midrapidity than spectrometer's; therefore $dN/d\eta$ is measured over different ranges of $\eta$. I had to involve RQMD simulation to be able to compare $dN/d\eta$ from the Si and the spectrometer. In principle one can get the same answer from the measurement of non-identified $dN/dy$ distribution for + and − (like NA49's $h^-$ [10]).

Therefore I require that the absolute $dN/\,d\eta$ in Si and spectrometer match with factors which I derive from RQMD distribution, see Table 2.2. The spectrometer acceptance was cut down to a fiducial range, free of the edge effects (monitored by the acceptance-corrected $dN/\,d\eta$ histograms with high resolution in $\eta$). These factors are the ratios of $dN/d\eta$ from the simulation alone. The simulation needs to know only the gross shape of $dN/d\eta$ for both signs, which RQMD does know. (Its $dN/dy$ distribution for pions has $\sigma = 1.4$ in agreement with NA49 $h^-$ [10]. ) The words "simulation alone" mean that delta electrons which I do not simulate, as well as imperfections of Si alignment, which I do not know, do not affect the simulated factors. Massive particles have asymmetrical $dN/d\eta$ distribution and our high angle spectrometer settings cover them more efficiently than Si. As a result, the simulated factors are different for + and − because of the asymmetry between protons/antiprotons and $K^+/K^-$.

| $\frac{spectrometer}{Si(+and-)/2}$ | Spectrometer sign | |
|---|---|---|
| | $+$ | $-$ |
| high angle | 1.208 | 0.986 |
| low angle | 1.025 | 0.871 |

Table 2.2: RQMD-generated factors for acceptance matching. The following acceptance intervals were used. For the Si: $\eta_{min} = 1.5$, $\eta_{max} = 3.3$. For the spectrometer: in the low angle setting, $\eta_{min} = 3.6$, $\eta_{max} = 4.4$. In the high angle setting, $\eta_{min} = 2.6$, $\eta_{max} = 3.1$.

### 2.2.7 $dN/d\eta$ comparison: Si vs spectrometer

In my method I scan correlation between the normalized (under some tentatively assumed trigger centrality) spectrometer $dN/d\eta$ of non-identified tracks and the Si $dN/d\eta$. Acceptance correction for the non-identified spectrometer tracks is described in subsection 2.1.4. The spectrometer $dN/d\eta$ is corrected for the inefficiencies due to dead channels, presence of the pad chamber in the trigger, tracking confidence level cuts, and includes extrapolation to $p_T = \infty$. The correlation is scanned varying the T0 multiplicity, with 14 fixed T0 thresholds. Accepted is the centrality that makes spectrometer and Si $dN/d\eta$ match with the factors shown in the Table 2.2. An example of such centrality fitting is illustrated by Fig. 2.1 and Fig. 2.2.

Shown in the right part of Fig. 2.1 is the "diagonalized" T0 distribution

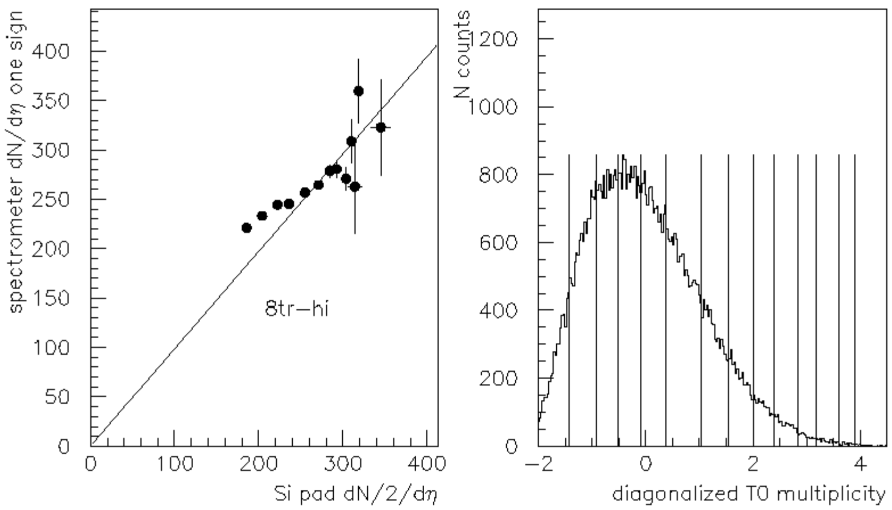


Figure 2.1: Left: correlation between $dN/d\eta$ obtained by charged track counting in the spectrometer and fired pad counting in the Si, found to be the best for a particular spectrometer setting. Right: positions of the multiplicity bins of the left plot along the “diagonalized” and normalized T0 amplitude.

from two PMT tubes on the $\delta$-free side. (The "diagonalization" means that distributions from two tubes on the $\delta$-free side were gainmatched, the covariance matrix that describes their correlation was diagonalized, and the value plotted is the diagonalized coordinate which is correlated with multiplicity.) The points shown correspond to 14 centrality bins with boundaries 0, .0001, .0002, .0005, .001, .0025, .005, 0.01, 0.02, 0.04, 0.06, 0.08, 0.10, 0.12, 0.14, later referred to as $c_i$. Of course, the thresholds $t_i$ change with different values assigned as the overall trigger centrality. The vertical lines across the T0 distribution in the right panel of Fig. 2.1 show locations of the thresholds which maximize the correlation in the left panel.

Fig. 2.2 justifies why the correlation on Fig. 2.1 was found to be maximized by the centrality chosen. It shows the $\chi^2$ (per number of degrees of freedom) between each of three possible correlations and the one expected on the basis of acceptance simulation (see Table 2.2), vs the number of points involved. Data for three close choices of centrality are shown, the best choice is the one plotted by ○.

The trend present on most figures like Fig. 2.1, left, (analyzed separately for every spectrometer setting) is a flattening of the correlation slope for lower multiplicity bins, as compared to a perfect correlation, especially for those *bins* where central T0 distribution deviates significantly from the valid beam one. The centrality thresholds are chosen based on the interpolation of the integrated T0 amplitude distribution $dN/dA$,

$$f(t) = \int_t^\infty \frac{dN}{dA}\, dA,$$

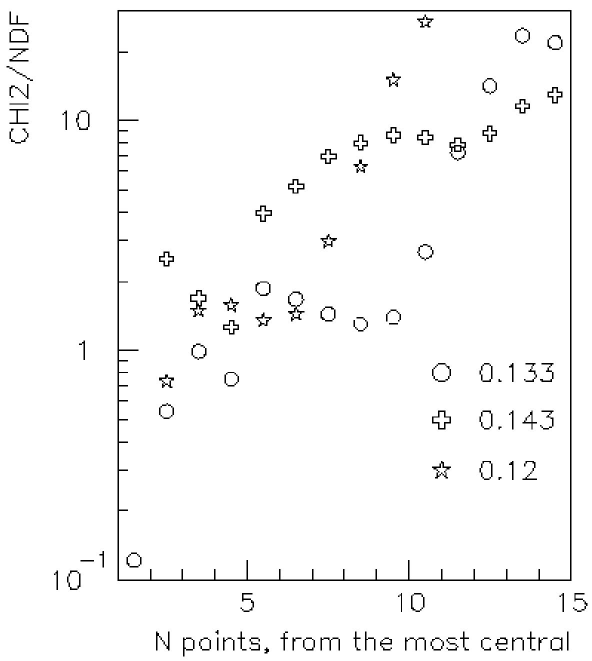


Figure 2.2: $\chi^2/NDF$ between actual correlations and the one expected on the basis of acceptance simulation, vs the number of points involved, for three different centralities.

where $dN/dA$ is normalized so that $f(-\infty) = c$. Recall that these runs are central triggered. Normalization of every run period is done with $dN/dA$ of that period, i.e. the physics runs are normalized using their own $dN/dA$. The above mentioned 14 thresholds $t_i$ come from solving numerically the 14 equations

$$f(t_i) = c_i. \tag{2.26}$$

From this it is clear that the bins to the left of the maximum in $dN/dA$ contain a broader composition of true centralities. However, the correlation in $dN/d\eta$ between the Si and the spectrometer holds as long as the tracks in the numerator of equation (2.16) come from events which are unbiased representatives of their centrality class. Recall here that both T0 and spectrometer, but not the Si, enter the trigger. Can we hope that the events in question are unbiased in this sense ? No, the bin contents to the left of the maximum in $dN/dA$ are the ones which deviate from the minimum bias T0 distribution *the most* ! Selection of these events is obviously the most affected by the trigger requirement of a spectrometer track. This explains why the correlation flattens out, i.e. the Si $dN/d\eta$ drops faster than the "same" quantity from the spectrometer.

### 2.2.8 Runs with Cherenkov veto

Clearly, the philosophy of the matching of non-identified $dN/d\eta$ can be implemented only for the runs with no Cherenkov veto. Statistics for kaons in pion runs is too low for meaningful analysis of physics as a function of centrality. One has to learn how to determine centrality of runs with the Cherenkov veto in the trigger. The way I do it is the following.

I link the T0 thresholds for the kaon run with chosen T0 thresholds in the nearby pion run by requiring bin-by-bin (in T0 bins) correlation of Si between the two runs. Once centrality of the pion run is known (by varying the centrality to optimize the correlation between spectrometer and Si $dN/d\eta$, as described in the previous section), the link to the pion run is provided by Si. Now I vary centrality of the kaon run $c_K$, thus vary T0 bin boundaries and optimize the correlation of Si with respect to Si – between the kaon and pion runs. The kaon run centrality that maximizes the correlation is accepted. In other words, the kaon and pion samples are normalized to each other using the Si; samples of *identical* Si multiplicity are

1. selected by proper choice of T0 thresholds
2. normalized using *identical* values of trigger centrality.

### 2.2.9 Correction for the consequences of radiation damage in Si

Radiation damage in Si detectors is known [11] to result in

- an increase in dark current due to damage to the bulk Si
- a decrease in the collected charge signal due to charge trapping

Both effects make discrimination of particle track signals against the noises and dark current background more difficult. Technically, the problem shows up in the number of hits with signal above the threshold, not associated with particle tracks. These "fake hits" affect the multiplicity measurement. The effect calls for evaluation and correction, which was done according to the following method:

1. In the valid beam run, a sample of "pure noise" Si events was selected by cuts on all T0 tubes, combined with a 2D cut on the Si amplitude sum vs Si number of hits, using both sides of the Si detector and vetoing Si events with large total amplitude (but not with large number of hits !). Thus the distribution of the number of hit Si pads (delta-free part only) in these "pure noise" events was sampled. It is an asymmetric distribution with maximum around 5 and a mean between 20 and 40, depending on the quality of the detector's performance. The asymmetry points to a "collective" nature of the effect responsible for the fake hits – in accordance with the features of the physics mechanism just discussed.

2. Knowing the "pure noise" distribution, and the "real+noise" distribution of the Si hits in the central trigger run, it is possible to reconstruct the "real" distribution, because the two known pieces of information determine it uniquely. The following "random purification" algorithm has been constructed:

   - make up a random number distributed according to the distribution of fake hits, $NFAKE$. Randomly pick $NFAKE$ Si channels.
   - make up a random number distributed according to the distribution of "real+fake" hits, $NTOTAL$.

- make up an integer random number uniformly distributed between 0 and the maximum number of working channels, $NPURE$. Randomly pick $NPURE$ channels.
- Count channel numbers occupied by $NPURE$ OR $NFAKE$.
- Compare it with $NTOTAL$.
- If it equals $NTOTAL$, histogram $NPURE$.
- Repeat the steps until sufficient statistics is obtained in the histogram of $NPURE$. By construction, the histogram so obtained represents the needed "rectified" distribution (with a caveat discussed below).

3. Transform the "real+noise" and "real" distributions into the Poissonian variable $\mu$ which characterizes multiplicity of tracks. Derive the correction factor, $\mu(real)/\mu(real + noise)$

4. Apply the correction directly to $dN/dy$

This ends the description of the correction method. Application of the method is illustrated by Fig. 2.3. [12]

---

[12] A caveat: the above described correction method is not rigorous because the simulation of effect is reduced to sampling from the distributions of observed $NTOTAL$ and $NFAKE$. In the procedure, $NTOTAL$ and $NFAKE$ are being sampled independently of each other. Useful pairs of $NTOTAL$ and $NFAKE$ are only those where $NTOTAL \geq NFAKE$. This means that the distribution of "useful" $NTOTAL$ and $NFAKE$, which will enter the correction procedure, will differ from

Table 2.3 gives the summary of corrections for all settings used in the analysis. The error bars on the correction factors were derived from the scatter of correction factors determined in 3 independent "random purification" runs, 1000 successful events each. Conclusions from the table:

1. Si in the the high angle setting performs better. This is natural, given the radiation damage mechanism of the problem, and the fact that the high angle setting was used earlier in the run.

2. As a general trend, the larger multiplicity bin (4%) needs less of a correction. This is because more real multiplicity leaves less room for the fake hits to contaminate the picture.

### 2.2.10 Results, systematic uncertainties, and conclusions.

The left and right halves of the Si detector had different number of working channels: 225 on the left side, 245 on the right, out of 256 on either side in total. In the analysis, a $\delta$-free side of the detector is used for each sign. This is the "left" (Saleve) side for the positive, and "right" (Jura) side for the negative settings. After the radiation damage correction (Table 2.3) is applied, a comparison of the so corrected multiplicities, measured in the samples of identical centrality by the left and right parts of the detector, is performed to test the quality of the multiplicity measurement. In all cases we look at $\delta$-free

---

the observable ones. However, in practice, for a central trigger run, in *most* cases $NTOTAL \gg NFAKE$. The result of this is that in case of the central runs, the bias coming from the condition $NTOTAL \geq NFAKE$ is negligible.

side, so it takes a change in the sign of magnetic field to compare the two sides. Fig. 2.4 shows the comparison where each point represents a particular setting of the Cherenkov trigger, angle and magnetic field strength. The abscissa and the ordinate represent average multiplicity of charged tracks, measured in the 4% centrality sample, in the positive and negative runs respectively, by one half of the detector. Corrections for the dead pads ($=\times 256/(256 - N_{dead})$) are applied. This comparison reveals a systematic trend for the right side of the detector to give somewhat higher multiplicity. Most likely this is due to geometrical misalignment which was not calibrated out in the '95 data set. The center of gravity of the set of points is displaced from the line representing the perfect correlation by about 5% of the typical multiplicity. This level of systematics seems acceptable.

The estimate of the systematic uncertainty in the centrality determination is based on the following considerations. Once the set of T0 thresholds at fixed centralities is established for every physics setting, a comparison of the Si multiplicities between different runs can be performed for every centrality bin. The variance of the Si multiplicity $dN/d\eta$ between different run periods (at fixed centrality) characterizes the uncertainty of the absolute normalization. Fractional error bar of $c$ is slightly better for high centrality points in agreement with my intuitive view that selection of high multiplicity samples and measurements of high multiplicity should be more reliable, because statistical fluctuation of a larger number is relatively smaller. For the interesting range of centralities ($c \leq 0.1$) the $\sigma(c)/c = 0.06$. For kaons, because the Si is involved twice, I multiply the above mentioned centrality uncertainty by $\sqrt{2}$.

Table 2.4 summarizes the centralities.

The advantage of this method of normalization is that it utilizes the Si *multiplicity* to solve the problem of normalization which is otherwise difficult to solve without making ungrounded assumptions, idealizing the experiment, e.g. the assumption that the top $x\%$ of T0 amplitudes are the top $x\%$ of the most central events, or that requirement of a spectrometer track in the trigger (with the "jaws" !) makes no effect on the centrality of the data sample so selected.

I have used RQMD simulation to link the acceptances of Si and spectrometer. I believe that any other normalization technique using T0 would, too, need simulations to fully understand the shape of minimum bias distribution in T0, and the effect of the spectrometer requirement in order to determine the trigger performance to the degree of realism needed for absolute normalization at the 6-8 % systematic error level. My approach reduces the simulation problem to the one which is quite tractable and relies on RQMD features not more sophisticated than the gross shape of $dN/d\eta$ distribution.

## 2.3 Track identification

A number of analysis steps have to be performed regardless of the particle identity one focuses on, and are common to $\pi$, $K$, etc. These are discussed in this section.

### 2.3.1 Double beam cut

The events of a beam particle crossing the target are distributed randomly in time, and there is a non-zero probability for more than one particle to come (and cause interactions) within a time interval shorter than our most sensitive equipment (i.e. the beam counters *BC*, see section 1.3.1) can resolve. This will look as a single event with abnormal properties, which we want to avoid. In the amplitude distribution of the PMT signals from the *BC*, one can clearly distinguish a secondary peak of the double beam events. The separation between the peaks is typically $3 \times FWHM$ of the single beam peak, so that clean discrimination is possible. The beam count $B$ in formula 2.17 is corrected to represent the fraction of events after the double beam cut has been applied. The fraction of rejected events was, depending on the setting, between 2.9% and 5.4%, and known with high precision.

### 2.3.2 Track confidence level cut

NA44 tracks particles in the volume behind the magnetic channel. In the *MUL1* (see subsection 1.3.3) runs, the predominant majority of events are single track ones, and our tracking situation is the simplest possible in a heavy ion experiment. Which devices are used to track particles, and which information they provide, is described in subsection 1.6.1. The tracks are fitted with straight lines in three dimensions. In the process, one obtains two $\chi^2$ values (vertical and horizontal), which, for given number of degrees of freedom $NDF$, characterize the quality of the fit. For given $\chi^2 = X$ and $NDF$, we calculate the probability that a random variable from a true $\chi^2$ distribution with given $NDF$ happens to be larger than the given value $X$. We call this probability a *confidence level*, cut on it from below and call that a confidence level cut, or $CL$-cut. In experimental data (and in a realistic MC), due to a number of instrumental imperfections (detector off-set, fake hits, inefficiencies) and deviations of the real tracks from the idealistic fitting model (decays, conversions, multiple scattering) the percentage of tracks actually rejected by a sufficiently strict $CL$-cut is much higher than what the "nominal" value of the confidence level implies.

To get rid of the unreliable tracks in the off-line analysis of the experimental data, I rejected tracks with *either* vertical *or* horizontal $CL < 10\%$. To evaluate the probability for a real track to be lost as a result of that, I ran MC simulation (thus modelling some of the imperfections mentioned above), and found out that the combined $CL$-cut retains from 83% to 87% of the good tracks, slightly depending on the setting used. The respective correction (known with 4 digit precision) was applied for each setting.

### 2.3.3 Pad Chamber in the trigger

In the NA44 design upgraded for the *Pb* beam running, the PC is an essential tracking device of limiting acceptance. In 1995, a PC hit [13] was required in the multiplicity trigger. This increases the rate of useful events, but reduces the efficiency due to inherent inefficiency of the chamber and the

[13] read out by Gasplex

coincidence inefficiency. The following algorithm was used to find PC-related trigger inefficiency component:

1. Count good tracks in the run with PC in the trigger and normalize to the life beam.

2. Same in the run with no PC in the trigger, the rest of the trigger being the same

3. Take the ratio; apply as a multiplier to the particle yield.

If a couple of data sets with the trigger conditions required for the comparison could not be found, we used the one with the closest settings. Table 2.5 summarizes the corrections.

## 2.4 Pion identification

Here I discuss the issues specific to pion identification. Success of the UCAL calibration (whose usefulness had been hitherto limited by effects of radiation damage in the scintillator) enabled a correction for the inefficiency of pion PID due to a Cherenkov ($C2$) veto. This made it possible to obtain normalized yields of $\pi^+$ and $\pi^-$ published in [12] and discussed in Chapter 3. Table 2.4.2 summarizes the coditions necessary to identify a track as a pion, in addition to those necessary to validate a track and described in Section 2.3.

### 2.4.1 Time of flight in pion identification

In the weak field setting, time of flight is helpful in separating pions from kaons. The principles of particle identification by the TOF cut and of performance evaluation for such a cut are discussed in subsection 2.5.1 and are not different for pions.

### 2.4.2 UCAL calibration

The calibration was performed using the standard technique, documented eslewhere [13] and based on the measurement of Uranium's natural radioactivity via the scintillator stack. As a rule, the dedicated calibration measurements were taken before and after the physics running session. The pedestals were extracted from the out-of-burst information found on physics tapes. The time stability of the calibration constants over the period of $Pb$ beam running was 5-10%, with a clearly seen systematic trend for the later calibration to give larger calibration constants. Stability of the pedestals was better than 0.5%.

The DST software innovations were caused by the need of coping the problem of *radiation damage* in the scintillators. The radiation damage is known [14] to result in significant absorption of light in the scintillators and observable (factor of 2 in our device) dependence of the signal amplitude on the location of primary track. Hitherto, this problem had not been addressed in the NA44 DST production software.

The correction method chosen consisted in constructing a product of the two PMT amplitudes for each tower. The way it affects usage of the calibration constants is a subject of a special discussion and therefore is separated in Appendix A. In brief, to recalibrate, one must multiply tower's energy by a factor which depends on the attenuation length and therefore has to be measured. The measurement was performed by selecting the tower with maximum amplitude (to be able to ignore the effects of threshold and pedestal subtraction, the random details of propagation of shower tracks to the neighbooring towers and sharing of light between the towers), then averaging separately the sum and the product of the tower's two PMT signals, and taking the ratio of sum/product. Only single track events were considered. Under some model assumptions, one can relate this ratio to the attenuation length in the scintillator. [14]

I estimated the attenuation length to be between 5 and 7 cm for most of the towers in 1996. It was seen to be systematically shorter in the EM section (which had no Cu plates in it [5]). The pure U stacks showed better performance and therefore seemed to had been restacked with newer scintillator. Comparing the sum/product ratios between 1995 and 1996, I noticed a systematic increase of about 5-7% in 1996, which indicated continuing detereoration.

A potential danger associated with using the product is that of losing the signal altogether if at least one of the PMTs gives no signal, as may happen due to the attenuation. However, the counterargument is that this never happens for (nominal spectrometer momentum) electrons in the EM

[14]as discussed in detail in Appendix A

section and hadrons in the hadronic section. Therefore, the possibilities of identifying the electromagnetic events by high EM signal, selecting hadrons by high signal in the hadronic section and vetoing any garbage by low signal remain unaffected. I studied the issue quantitatively, selecting (by Cherenkovs, *C2* at 14.7 PSI) a sample of electrons and a sample of protons and kaons in a 4 GeV positive setting, and found that for the true electrons the inefficiency due to making a product instead of a sum is $(0.2 \pm 0.1)\%$, which is comparable with the inefficiency due to non-interacting $\exp(-6.4)$. For $p$ and $K$, such kind of inefficiency in the hadronic section is less than $1 \times 10^{-4}$ due to the larger signal from these particles.

Out of variety of other possible correction methods, the two had been tried:

1. correction based on comparison of the left and right PMT signals

2. correction based on the external tracking

I concluded that it would be more difficult to achieve a performance comparable to that of the product method using 1) or 2) or their combination.

### 2.4.3 Correcting for the electron veto inefficiency.

The problem of electrons misidentified as pions is non-neglegible in the low field settings only, because the spectrum of electrons falls rapidly with momentum. The electron veto correction factor was determined using supplementary PID provided by the UCAL electromagnetic/hadronic ratio. The question of how tight a cut one needs to apply in order to get the supplementary PID is of little importance, since the electron veto inefficiency determination operates entirely *within* the sample which satisfies this tough PID criterion. This is true as long as devices used for the veto and for the supplementary PID are uncorrelated. The requirement of $UCHAD/UCEM > 10$ identifies track as a reliable hadron and constitues the tough, clean supplementary PID. Fig. 2.5 shows how the ratio of tracks that exceed the pion $C2$ veto cut to those that do not (let me denote this as $N(\bar{C}2)/N(C2)$) changes with $UCHAD/UCEM$. Such figures were obtained for all low field settings and different centralities. They all have the same characteristic pattern: the ratio falls with $UCHAD/UCEM$, and then becomes flat after $UCHAD/UCEM$ exceeds a certain threshold[15]. From this we conclude that

- a high signal in $C2$, just as a low ratio $UCHAD/UCEM$, both characterize the same group of tracks – obviously, the $e^+(e^-)$ ones

- contribution of the $e^+(e^-)$ goes down to zero when $N(\bar{C}2)/N(C2)$ gets flat, and thus one chooses the safe $UCHAD/UCEM$ cut

- for true hadrons, the reasons that cause $C2$ to fire are unrelated to UCAL since $N(\bar{C}2)/N(C2)$ is flat above 10.

[15]This was not seen until I calibrated out the position dependence of the UCAL signal, significant due to the radiation damage in the scintillator (see Subsection 2.4.2).

Thus we have justified the electron veto correction obtained via UCAL. It is the factor

$$1 + N(\bar{C2})/N(C2) \tag{2.27}$$

with the counting errors in both $N$ counts propagating into the systematic error of the pion yields.

### 2.4.4 Counting pions in the strong field setting.

In the strong field setting, to identify pions directly one needs to require a $C2$ firing (see Fig. 1.5 and discussion of the Cherenkovs in Subsection 1.3.4). However, it is desirable to avoid the uncertainty associated with the Cherenkov's efficiency, which would have entered the game had $C2$ been required to fire. Notice that sorting out $p$ ($\bar{p}$) off-line by vetoing $C1$ and $C2$ and using $TOF$ can be done cleanly and reliably even in the strong field settings. Having done that, we are left with a sample of $K$ and $\pi$[16]. For this sample, we can obtain distributions with respect to the kinematic variables of a $\pi$ by applying a pionic acceptance correction. Then, we obtain inefficiency-corrected, clean $K$ distributions with respect to the pionic $y$ and $k_T$, where a pionic acceptance correction is used. Finally, we subtract the kaon component in the disctributions:

$$\frac{dN(\pi)}{dy_\pi} = \frac{dN(\pi + K)}{dy_\pi} - \frac{dN(K)}{dy_\pi} \tag{2.28}$$

Needless to say that the $y$ above can be replaced by any kinematic variable.

[16]We neglect $e^+(e^-)$ for the reasons outlined in Subsection 2.4.3.

## 2.5 Kaon identification

Here I discuss the issues specific to kaon identification. Table 2.5 summarizes the coditions necessary to identify a track as a pion, in addition to those necessary to validate a track and described in section 2.3.

### 2.5.1 Time of flight in kaon identification.

The time of flight cut is used to separate $K^+, K^-$ from $p, \bar{p}$ respectively in the strong and weak field setting of the spectrometer at both arm angles. Since only particles with momenta within a narrow range are accepted by the spectrometer, [17] velocity

$$v = \frac{p}{\sqrt{m^2 + p^2}} \tag{2.29}$$

becomes a measure of particle's mass $m$. $v$ itself is measured by time interval between the interaction (provided by beam counter [18]) and the scintillation hodoscope *H3*. [19] $K/p$ sepatation is therefore achieved by a TOF cut. A good cut is slat dependent as velocity and slat number are correlated by virtue of the spectrometer's analyzing power. The problem of this cut's cleanliness/efficiency becomes noticeable only in the strong momentum setting. By *performance evaluation* I mean a procedure which allows me to answer two questions:

[17] data on momentum acceptance is found in Table 1.2

[18] see section 1.3.1 for description

[19] see section 1.3.1 for description

- how many real particles get lost due to the cut?
- how many unwanted ones get misidentified ?

The TOF distribution is Gaussian and therefore easy to analyze. The algorithm consists of the following steps:

1. Select a sample of tracks of desired PID, using *all* cuts except for the hodoscope cut.
2. For this sample, fill sepatate TOF histograms for every slat.
3. Fit each slice with a sum of two Gaussians; assume that TOF distribution is independent of PID and take the sigmas to be the same.
4. For the two Gaussians with known separation, find the contamination and the loss due to the cut.

The corrections can be found in Table 2.5.

### 2.5.2 Correcting for pion/electron veto inefficiency

At this point we turn again to the figures (Fig. 1.4 and Fig. 1.5) that illustrate the difference in the approaches to kaon identification in different spectrometer settings. As was already discussed in Section 1.3, a Cherenkov veto ($\bar{C}$) was used to obtain kaon-enhanced data samples. The price of the high cleanliness of a PID with $\bar{C}$ is its high inefficiency: any event resulting in a firing of the vetoing Chereknov's counter (a passage of any charged particle of sufficient velocity through the counter's aperture ) may result in a loss of a kaon. To evaluate this inefficiency, we take the following steps:

1. On-line: obtain a sample with the veto lifted and a sufficient statistics of kaons.

2. Off-line: in the sample with the veto lifted, find a way of *counting* [20] the kaons with and (non-trivial !) without the veto.

The counting of the rejected kaons can be possible in presense of a device sensitive to the difference between kaons and lighter particles. Presense of a device capable of *identifying* kaons independently of the Cherenkovs is ideal. Such an ideal case is realized in the weak magnetic field setting, (see Fig. 1.4) where the $m^2$ measurement (due to the good time-of-flight resolution) allows one to tell kaons from lighter particles even in the absense of the veto. The inefficiency correction factor is therefore easily calculable:

$$1 + \frac{N(K)_{lost}}{N(K)_{detected}} \tag{2.30}$$

The case of a strong field setting (see Fig. 1.5) is complicated by the fact that a particle lost due to the veto is not necessarily a kaon, but a kaon or a lighter particle. The lighter particle is most likely a pion and will be called so in the following discussion. It is possible to *count* the lost kaons without identifying them, taking advantage of the fact that kaon and pion peaks in the $m^2$ spectrum of vetoed tracks (see Fig. 2.6) are well separated.

[20] To emphasise: we do not have to *identify*, but merely have to *count* the rejected kaons for this task.

In order to subtract the pions from all vetoed tracks, we select a clean sample of undoubtedly light tracks from a sample of good events with a single hit in hodoscopes $H2$ and $H3$ and only one reconstructed track, by requiring a large (characteristic of a pion) signal in $C1$. Since this requirement is highly selective, we use the shape of the distribution $dN_{clean,light}/\,dm^2$ so obtained, but not the magnitude of the probability it represents. Therefore, we seek a multiplier $\Upsilon$ that allows us to subtract the light particle distribution without remainder to obatain the number of the vetoed $K$ and $p$ only. We do it by dividng the "+" histogram on Fig. 2.6 by the clean light track distribution (not shown). Flatness of the ratio so obtained (shown as $\diamond$) is to be expectred in the range of $m^2$ where the light particle line shape selected is representative of the sample we want to subtract. We fit the ratio in the flat region to obtain the required multiplier $\Upsilon$, and subtract the light particle line shape:

$$\frac{dN(K+p)_{lost}}{dm^2} = \frac{dN_{lost}}{dm^2} - \Upsilon\frac{dN_{clean,light}}{dm^2} \tag{2.31}$$

The histogram plotted on Fig. 2.6 by $\circ$ represents the $m^2$ distribution of vetoed $K$ and $p$ only, $dN(K+p)_{lost}/\,dm^2$. To get $N(K)_{lost}$, we pick an $m^2$ window (shaded on Fig. 2.6) and solve the standard problem of intepreting a sum of two Gaussian peaks as "signal" + "background", $K$ being the signal and $p$ the background.

## 2.6 Summary of the systematic uncertainties

Here I briefly summarize the systematic errors to the normalized yields and distributions of charged pions and kaons. For more detailed discussion see the appropriate section of this chapter. The systematic uncertainty in the calculation of the Cherenkov veto is dominated by the *statistical* uncertainty of the "lost" particle counting (see Eq. 2.30).

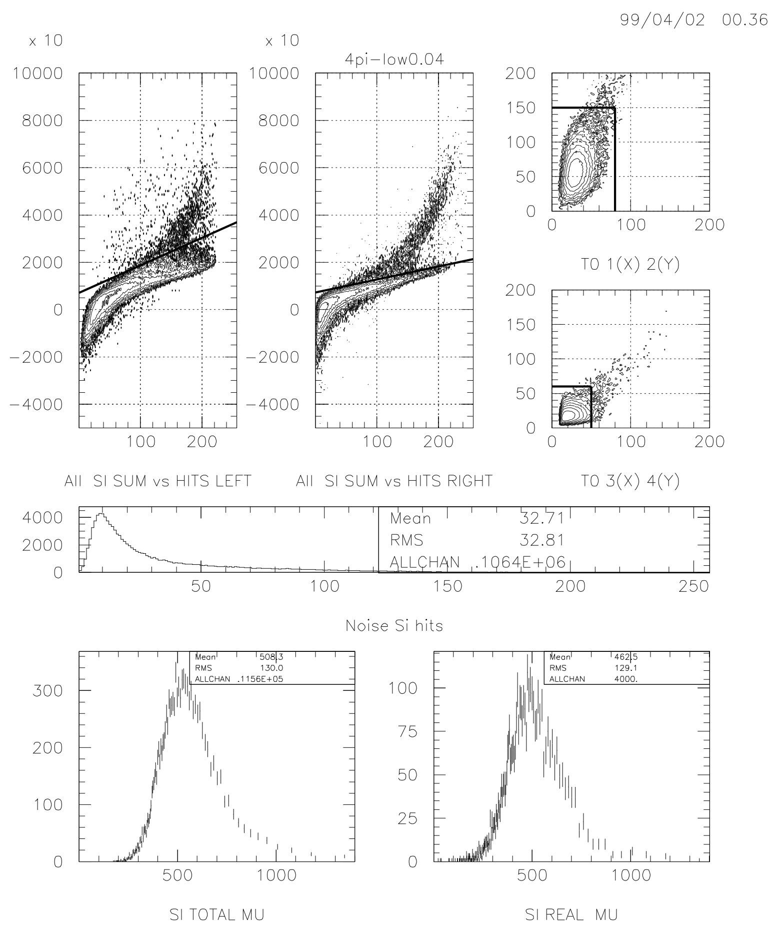


Figure 2.3: Illustration of the Si radiation damage correction algorithm in case of the 4GeV negative low angle setting, 4% centrality sample. From left to right, from top to bottom: SI ADC sum vs number of hits for the left and right parts of the detector in the valid beam run, with the non-interaction cut shown by the solid line; non-interaction cut on T0 signals in the valid beam run ; distribution of the number of Si noise hits in the valid beam run with the non-interaction cut; the “dirty” number of charged tracks ($\mu \times M$) in the physics run; the “purified” number of charged tracks $\mu \times M$. See text of Subsection 2.2.9

| Setting | 4% centr. | 10% centr | Setting | 4% centr. | 10% centr |
|---|---|---|---|---|---|
| 4k-low | 0.91 ± 0.013 | 0.902 ± 0.011 | 4k+low | 0.873 ± 0.002 | 0.864 ± 0.007 |
| 4k-high | 0.943 ± 0.004 | 0.951 ± 0.011 | 4k+high | 0.935 ± 0.008 | 0.931 ± 0.010 |
| $4\pi^-$low | 0.92 ± 0.01 | 0.921 ± 0.007 | $4\pi^+$low | 0.89 ± 0.02 | 0.876 ± 0.005 |
| $4\pi^-$high | 0.947 ± 0.002 | 0.934 ± 0.003 | $4\pi^+$high | 0.937 ± 0.01 | 0.934 ± 0.003 |
| 8k-low | 0.955 ± 0.004 | 0.955 ± 0.002 | 8k+low | 0.879 ± 0.013 | 0.879 ± 0.010 |
| 8k-high | 0.930 ± 0.003 | 0.926 ± 0.006 | 8k+high | 0.938 ± 0.005 | 0.947 ± 0.007 |
| $8\pi^-$low | 0.956 ± 0.008 | 0.948 ± 0.009 | $8\pi^+$low | 0.88 ± 0.016 | 0.872 ± 0.009 |
| $8\pi^-$high | 0.939 ± 0.008 | 0.9333 ± 0.0004 | $8\pi^+$high | 0.930 ± 0.013 | 0.931 ± 0.007 |

Table 2.3: Radiation damage correction. The factors listed here are applied directly to $dN/dy$.

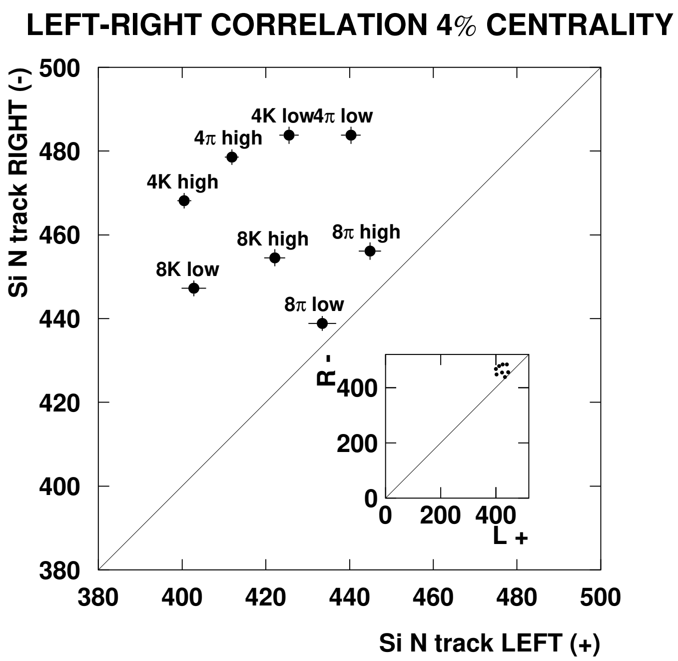


Figure 2.4: Comparison of the average charged track multiplicities measured independently by the left and right sides of the Si detector in the runs with different field sign. See text of Subsection 2.2.10.

| momentum | 4 GeV | | 8 GeV | |
|---|---|---|---|---|
| $p_T$ setting | low | high | low | high |
| $\pi^+$ | 0.145± 0.008 | 0.152 ±0.009 | 0.17 ±0.01 | 0.116±0.007 |
| $K^+$ | 0.145±0.011 | 0.152± 0.012 | 0.17 ± 0.014 | 0.116±0.009 |
| $\pi^-$ | 0.129± 0.007 | 0.128±0.007 | 0.143± 0.008 | 0.127 ±0.007 |
| $K^-$ | 0.129±0.010 | 0.128±0.010 | 0.145 ± 0.012 | 0.127 ± 0.010 |

Table 2.4: Trigger centrality $c$ of the physics settings.

| momentum | 4 GeV | | 8 GeV | |
|---|---|---|---|---|
| $p_T$ setting | low | high | low | high |
| $\pi^+$ | 1 | 1 | $1.13 \pm 0.01$ | 1 |
| $K^+$ | $8\pi^+$low | $8\pi^+$high | $8\pi^+$low | $8\pi^-$high |
| $\pi^-$ | 1.128 | 1 | $1.096 \pm 0.009$ | $1.219 \pm 0.011$ |
| $K^-$ | $4\pi^-$low | $8\pi^-$high | $8\pi^-$low | $8\pi^-$high |

Table 2.5: Corrections for the PC in the trigger. "1" is used when PC was not part of the trigger. See section 2.3.3.

| setting | $C2$ | H3 | | $p_y, GeV/c$ |
|---|---|---|---|---|
| | | $a$, ns/slat | $b$, ns | |
| $4\pi^-$low | $\leq 58$ | .04 | 3 | $[.003, .008]$ |
| $4\pi^-$high: 3614,15,16 | $\leq 64$ | .04 | 3 | |
| $4\pi^-$high: 3617,18 | $\leq 64$ | -.04 | -2 | |
| $4\pi^+$low | $\leq 74$ | .03 | 3 | $[0.002, 0.008]$ |
| $4\pi^+$high | $\leq 74$ | .05 | 2 | |
| $8\pi^-$low | see text | .04 | 4. | $[0.006, 0.01]$ |
| $8\pi^-$high | see text | .04 | 4. | |
| $8\pi^+$low | see text | .04 | 4. | $[0.006, 0.01]$ |
| $8\pi^+$high | see text | .04 | 4. | |

Table 2.6: Summary of conditions used to identify a track as a $\pi$ (PID cuts). The "$4\pi^-$high" setting was split in two because of different hodoscope calibrations. The $a$ and $b$ parameters are used to specify a slat-dependent hodoscope cut: $H3TOF < H3SLAT \times a + b$, where $H3TOF$ is time-of-flight, $H3SLAT$ is the slat number. Words "see text" refer to Subsection 2.4.4. The fields are left blank when a device was not used to apply a cut for the $\pi$ identification.

| setting | Cherenkov veto correction | | H3 TOF |
|---|---|---|---|
| | 10% | 4% | |
| $4\pi^-$low | 1.93 ± 0.07 | 1.94 ± 0.07 | 1 |
| $4\pi^-$high | 1.239± 0.014 | 1.23 ± 0.02 | 1 |
| $4\pi^+$low | 1.57 ± 0.05 | 1.59 ± 0.08 | 0.996 |
| $4\pi^+$high | 1.096± 0.006 | 1.11 ± 0.01 | 1.021 |
| $8\pi^-$low | N/A | N/A | 1 |
| $8\pi^-$high | N/A | N/A | 1 |
| $8\pi^+$low | N/A | N/A | 0.9936 |
| $8\pi^+$high | N/A | N/A | 0.9957 |

Table 2.7: Corrections to the $\pi$ yields related to the process of particle identification for the samples of top 10% and top 4% centrality.

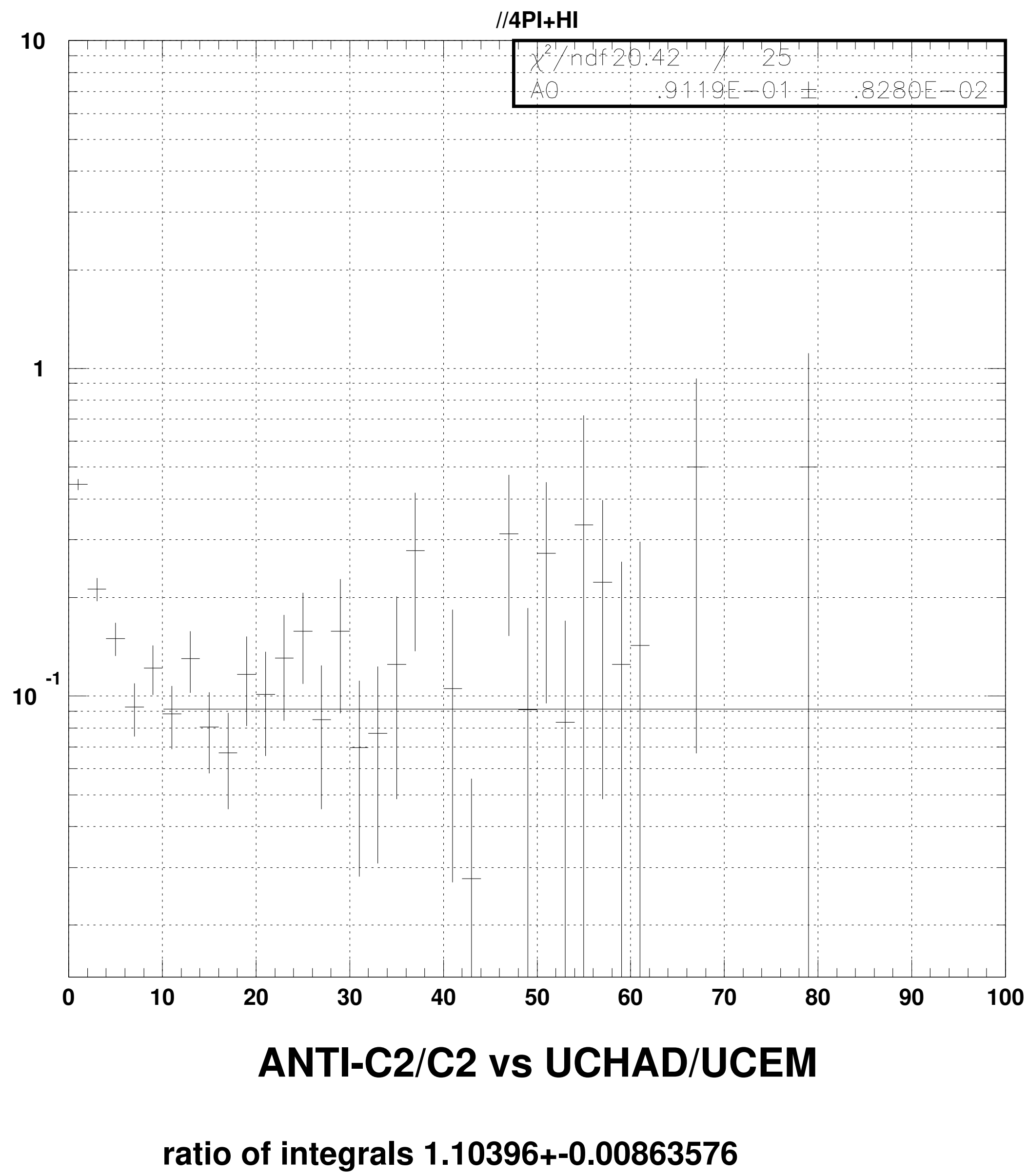


Figure 2.5: $N(\bar{C}2)/N(C2)$ (see text of subsection 2.4.3) as a function of $UCHAD/UCEM$ for the weak field, high angle, positive polarity setting.

| setting | $C1$ | $C2$ | H3 | | H2 | | $p_y, GeV/c$ |
|---|---|---|---|---|---|---|---|
| | | | a | b | a | b | |
| $4K^-$low | ≤70 | ≤60 | .1 | 10 | 0. | 10 | $[0.002, 0.009]$ |
| $4K^-$high | ≤77 | ≤74 | .1 | 10 | .083 | 7 | |
| $4K^+$low | ≤75 | ≤65 | .1 | 10 | | | $[0.002, 0.009]$ |
| $4K^+$high | ≤77 | ≤74 | .1 | 10 | | | |
| $8K^-$low | | ≤59 | .067 | 1.5 | | | $[0.006, 0.01]$ |
| $8K^-$high | | ≤63 | .05 | 2. | | | |
| $8K^+$low | | ≤59 | .067 | 1.5 | | | $[0.006, 0.012]$ |
| $8K^+$high : $K$ calibr | | ≤66 | .06 | 1. | | | |
| $8K^+$high : $p$ calibr | | ≤66 | -.06 | -1.5 | | | |

Table 2.8: Summary of conditions used to identify a track as a $K$ (PID cuts). The "$8K^+$high" setting was split in two because of different hodoscope calibrations. The $a$ and $b$ parameters are used to specify a slat-dependent hodoscope cut: $H3TOF < H3SLAT \times a + b$, where $H3TOF$ is time-of-flight, $H3SLAT$ is the slat number. The fields are left blank when a device was not used to apply a cut for the $\pi$ identification.

| setting | Cherenkov veto correction | | H3 TOF |
|---|---|---|---|
| | 10% | 4% | |
| $4K^{-}$low | 2.2 ± 0.7 | 3.1 ± 0.8 | N/A |
| $4K^{-}$high | 1.46± 0.05 | 1.56± 0.09 | N/A |
| $4K^{+}$low | 2.61± 0.21 | 2.91± 0.34 | N/A |
| $4K^{+}$high | 1.22± 0.04 | 1.20± 0.05 | N/A |
| $8K^{-}$low | 2.08± 0.16 | 2.4 ± 0.6 | 1.056 |
| $8K^{-}$high | 1.10± 0.04 | 1.09± 0.04 | 1.016 |
| $8K^{+}$low | 2.15± 0.12 | 2.4 ± 0.4 | 1.086 |
| $8K^{+}$high | 1.12± 0.01 | 1.15± 0.05 | 1.0028 |

Table 2.9: Corrections to the $K$ yields related to the process of particle identification for the samples of top 10% and top 4% centrality.

Figure 2.6: Obtaining the inefficiency correction for the Cherenkov veto in the strong field case. The number of rejected kaons is evaluated by subtracting the clean pion $m^2$ line shape scaled by a proper multiplier $\Upsilon$. $+$ – all vetoed tracks $dN_{lost}/\,dm^2$; $\diamond$ – ratio of the pure pion line $dN_{clean,light}/\,dm^2$ to the "all vetoed tracks" distribution, $\circ$ – $dN(K+p)_{lost}/\,dm^2$ obtained as "all vetoed tracks" minus $\Upsilon$ - scaled pion line (see Eq. 2.31).

# Chapter 3

## Inclusive single particle results for $\pi$ and $K$.

## Their meaning.

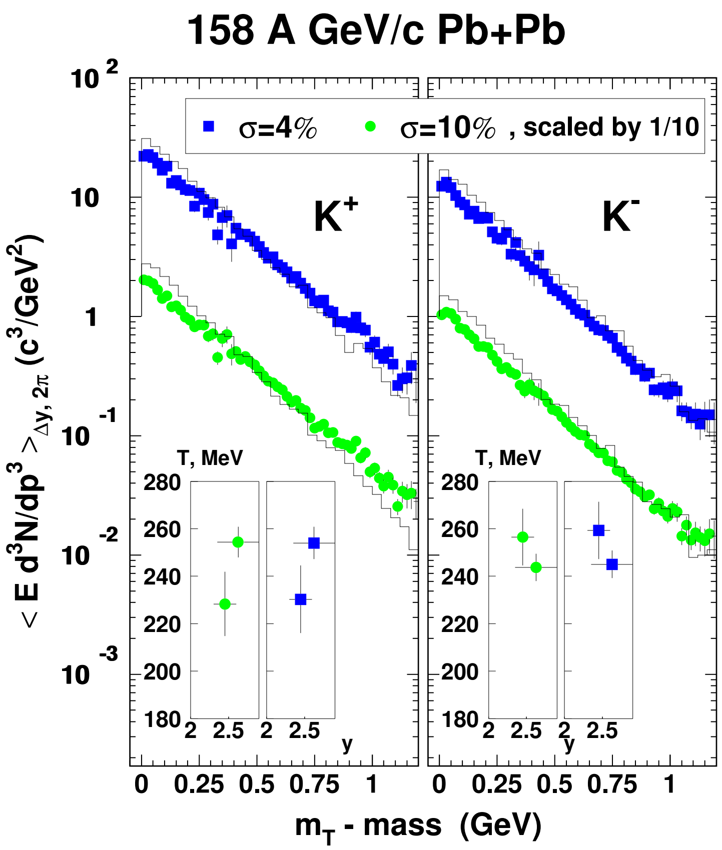


Figure 3.1: Measured transverse kinetic energy distributions of positive and negative kaons for the 4% and 10% most central of Pb+Pb collisions. Two spectrometer angle settings meet at $m_T - m = 0.35$ GeV. The fits follow the form $1/m_T\, dN/\, dm_T \propto exp(-m_T/T)$, where $m_T = (m^2 + p_T^2)^{1/2}$. $y$ ranges of the fits are given in Table 2 and are indicated by the horizontal errorbars in the inserts. RQMD predictions for $|y - y_{CM}| < 0.6$ (i.e., within NA44 acceptance) are shown as histograms.

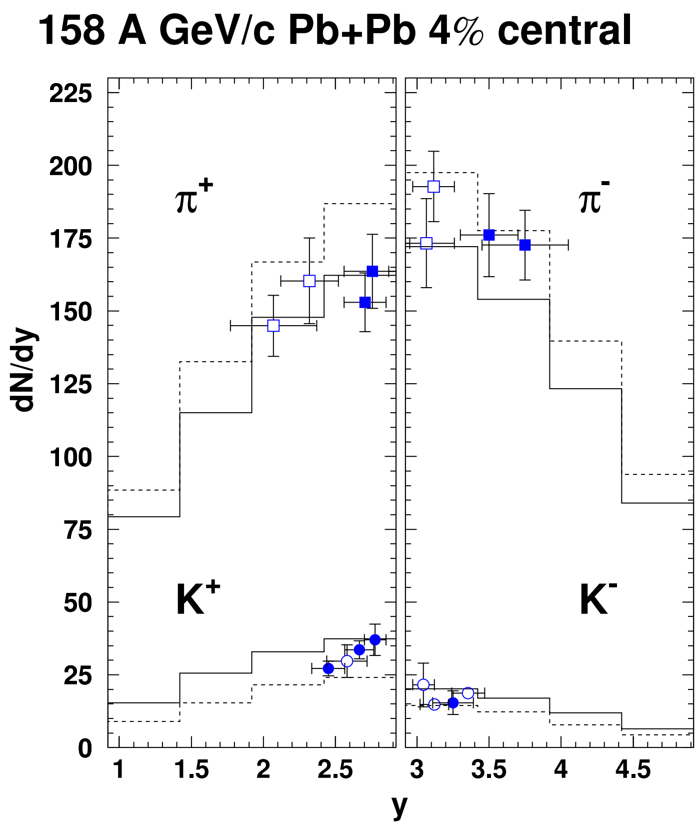


Figure 3.2: Comparison of measured charged kaon and pion yields with RQMD predictions. The vertical error bars indicate statistical and systematic errors, added in quadrature; the horizontal ones – $y$ boundaries of the acceptance used for $p_T$ integration in each spectrometer setting. Open symbols represent spectrometer settings whose $y$ position is shown mirror-reflected around midrapidity (2.92); their solid analogs – the actual settings. RQMD: solid line – standard mode, dashed line – no rescattering.

| PID | $y$ interval | $T$ (MeV) | $\sigma(T)$ stat., syst. (MeV) |
|---|---|---|---|
| $K^+$ | 2.3-2.6 | 230 | $\pm$ 8 $\pm$ 14 |
| $K^+$ | 2.4-2.9 | 254 | $\pm$ 4 $\pm$ 7 |
| $K^-$ | 2.3-2.6 | 259 | $\pm$ 8 $\pm$ 12 |
| $K^-$ | 2.4-2.9 | 245 | $\pm$ 7 $\pm$ 6 |

Table 3.1: Inverse slope parameters T.

| PID | $y$ interval | $dN/dy$ | $\sigma(dN/dy)$ | PID | $y$ interval | $dN/dy$ | $\sigma(dN/dy)$ |
|---|---|---|---|---|---|---|---|
| $K^-$ | 2.7-2.9 | 21.5 | $\pm$ 7.5 | $K^+$ | 2.7-2.9 | 37.1 | $\pm$ 5.4 |
| | 2.3-2.5 | 18.7 | $\pm$ 1.9 | | 2.3-2.6 | 27.2 | $\pm$ 2.5 |
| | 3.1-3.4 | 15.4 | $\pm$ 4.1 | | 3.1-3.4 | 29.7 | $\pm$ 5.6 |
| | 2.6-2.8 | 14.8 | $\pm$ 1.4 | | 2.6-2.8 | 33.6 | $\pm$ 3.1 |
| $\pi^-$ | 3.3-3.7 | 176 | $\pm$ 14 | $\pi^+$ | 3.3-3.7 | 160 | $\pm$ 15 |
| | 2.6-2.9 | 193 | $\pm$ 12 | | 2.6-2.9 | 153 | $\pm$ 10 |
| | 3.5-4.0 | 173 | $\pm$ 12 | | 3.5-4.0 | 145 | $\pm$ 10 |
| | 2.6-2.9 | 173 | $\pm$ 15 | | 2.6-2.9 | 164 | $\pm$ 13 |

Table 3.2: Particle distributions in rapidity for top 4% centrality. Every spectrometer setting provides an independent measurement. Settings overlapping in $y$ are listed separately. Statistical and systematic errorbars are added in quadrature to form $\sigma(dN/dy)$ listed.

# Bibliography


[1] Review of Particle Properties, Phys. Rev. D45, Part 2 (1992)

[2] N. Maeda *et al.*, NIM A346 (1994) 132-136

[3] E. Beuville *et al.*, NIM A288 (1990) 157-167

[4] E. Chesi, P. Martinengo, Digital Read-out for Analog Multiplexing Signals, CERN, 1988.

[5] T. Akesson *et al.*, NIM A241 (1985) 17-42

[6] R. Klanner, NIM A235 (1985) 209]

[7] T. Kobayashi, T. Sugitate, NIM A287 (1990) 389-396

[8] M. Spegel. Cathode Pad Chambers on the Trail of the Quark-Gluon Plasma. Master's Thesis. Institute für Kernphysik, Technische Universität Wien. November 1994.

[9] V.B.Berestetsky, E.M.Lifshitz, L.P.Pitaevsky, Quantum Electrodynamics.

[10] NA49 Collaboration, Nucl. Phys. A610(1996) 188c-199c

[11] H. Dietl et al, NIM A253 (1987) 460-466

[12] NA44 Collaboration, Phys. Lett. B471(1999) 6-12

[13] Y.Sirois, Ph.D. thesis

[14] Y.Sirois, R.Wigmans. NIM A240 (1985) 262-274

# Appendix A

# Re-calibrating UCAL to correct for the light absorbtion.

The algebra here provides technical background for the material discussed in 2.4.2. By $A$ and $C$ I denote the amplitude and calibration constant in case of no light absorbtion, and by $a$ and $c$ – the actual ones, respectively. If the light intensity in scintillator gets attenuated with distance $x$

$$a = Ae^{-x/L},$$

and the scintillator length is $S$, then the amplitude observed in a single channel (averaged over all positions in $x$ and eliminating the pedestal) is not $A$ as it were in the absence of attenuation, but $a = AL/S(1 - \exp(-S/L))$. Each UCAL tower is served by two PMT tubes, so we have $a_1$ and $a_2$; their gains are matched so that $< a_1 >=< a_2 >$. Calibrating a channel [1], I require that

$$(A_1 + A_2)L/S(1 - \exp(-S/L))c = E_0, \tag{A.1}$$

[1] in a dedicated run where natural radioactivity of U is measured by the scintillator

where $c$ is to be determined and $E_0$ is known. We will denote $(A_1 + A_2)C$ as $E_{cal}$ to indicate that this is the energy observable which we know how to calibrate. [2]

The left and right PMT register the light which passes the distance $x$ and $S - x$, respectively (if the source is point-like). We use the product of the two so that our new observable is

$$E_{\times} = c\sqrt{A_1 e^{-\frac{x}{L}} A_2 e^{-\frac{S-x}{L}}} = c\sqrt{A_1 A_2} e^{-\frac{S}{2L}} \tag{A.2}$$

It is independent of $x$, but has yet to be calibrated, i.e. related to $E_{cal}$. Next we notice that $C = cL/S(1 - \exp(-S/L))$ from A.1, and that in the absense of absorption for the gain-matched tubes $\sqrt{A_1 A_2} = (A_1 + A_2)/2$, and therefore

$$E_{\times} = \frac{\exp(-S/2L)}{2L/S(1 - \exp(-S/L))}(A_1 + A_2)C = \frac{< \sqrt{a_1 a_2} >}{< a_1 + a_2 >}(A_1 + A_2)C, \tag{A.3}$$

where we recognized that the $S$ and $L$-dependent prefactor can be expressed in terms of the easily measurable averages. This means that calibration can be restored for the product with the help of the expression:

$$E_{\times} = \frac{< \sqrt{a_1 a_2} >}{< a_1 + a_2 >} E_{cal} Byitself, thisresultisnaturalandpredictable. Itsvalueliesinthefactthatabsorbtionlengthisnowrelatedtoobservables. \tag{A.4}$$

[2] if not for the light attenuation, it would have been sufficient.